

Numerical Simulation of Parametrically Excited Bistable MEMS Plates

DIPLOMA THESIS

submitted in partial fulfillment of the requirements for the degree of

Diplom-Ingenieur

in

Embedded Systems

by

Johannes Fabian, BSc

Registration Number 01429210

to the Faculty of Electrical Engineering and Information Technology

at the TU Wien

Advisor: Univ.Prof. Dipl.-Phys. Dr.rer.nat. Ulrich Schmid

Assistance: Univ.Ass. Daniel Platz, MSc PhD

Vienna, 2nd September, 2022

Johannes Fabian

Ulrich Schmid

Declaration of Authorship

Johannes Fabian, BSc

I hereby declare that I have written this Diploma Thesis independently, that I have completely specified the utilized sources and resources and that I have definitely marked all parts of the work - including tables, maps and figures - which belong to other works or to the internet, literally or extracted, by referencing the source as borrowed.

Vienna, 2nd September, 2022

Johannes Fabian

Acknowledgements

First, I want to thank Univ.Prof. Dr. Ulrich Schmid for the opportunity to contribute to the research in the division of Microsystems Technology at the Institute for Sensor and Actuator Systems, and for the support I received during my work.

I want to express my biggest gratitude to my supervisor Dr. Daniel Platz for the exceptional collaboration on the journal article accompanying this diploma thesis and his mentorship during the whole project. Your enthusiasm and never ending inquisitiveness always inspired me and made this work one of the biggest learning experiences I have ever had. Our discussions and meetings have helped me many times when I felt stuck and made it easier to work through the complex theory this thesis encompassed.

There are a lot of colleagues that made my time at the TU Wien interesting and enjoyable. I want to especially thank my colleague and friend Thomas Ballon for all the memorable hours we spent studying and the many liters of coffee we shared.

For always being there for me and all the support and encouragement I want to thank my girlfriend Alina. Thank you for always having my back.

Finally I will always be grateful to my parents Gerlinde and Edmund for their support during my studies. Thank you for enabling me to truly savor this chapter of my life.

Kurzfassung

Mikroaktuatoren, die bistabile MEMS-Membranen und piezoelektrische Ansteuerung verbinden, sind ein spannendes aktuelles Forschungsthema auf dem Gebiet der Mikrosystemtechnik. Die Bistabilität von MEMS-Membranen wird durch eine hohe statische mechanische Vorspannung erreicht, die oftmals aus dem Herstellungsprozess resultiert. Oberhalb einem kritischen Wert der Vorspannung bilden sich in der Membran zwei stabile Knickzustände (Buckling). Durch eine periodische Anregung einer piezoelektrischen Schicht auf der Membran wird die mechanische Spannung in der Membran dynamisch verändert, wodurch Schwingungen angeregt werden, die zu einem Umschalten der Membran führen können. Um die hohen Auslenkungen, die diese Systeme als Aktuatoren interessant machen, nutzen zu können, muss dieser nichtlineare Umschaltprozess genau verstanden werden. Dazu wird in dieser Arbeit ein mathematisches Modell auf Basis der von-Karman-Plattengleichung eingeführt. Mit Hilfe der Galerkin-Methode wird die zeitabhängige Auslenkung der Platte als Superposition einer beliebigen Anzahl an Schwingungsmoden dargestellt, wodurch das Problem auf ein System gekoppelter nicht-linearer gewöhnlicher Differenzialgleichungen reduziert wird. Diese Gleichungen stellen die Bewegungsgleichungen für alle in Betracht gezogenen Moden dar. Das Gleichungssystem wird durch numerische Integration approximativ gelöst, wobei Geometrie- und Materialparameter ausgewählt werden, die relevant für typische MEMS-Bauelemente sind. Die numerischen Resultate zeigen, dass die statische Vorspannung einen starken Einfluss auf die multi-modale Umschaltdynamik der Membran hat. Außerdem betrachten wir den Einfluss des Anregesignals auf den Umschaltprozess. Hier zeigt sich, dass für eine Anregung mit nur wenigen periodischen Anregepulsen die Dynamik des Systems weniger komplex ist, wodurch kontrolliertes Umschalten erleichtert wird. Allerdings geht dies auf Kosten von höheren Signalamplituden, die nötig werden, um ein Umschalten der Membran hervorzurufen.

Abstract

Utilizing piezoelectrically excited bistable membranes as micro actuators is a novel topic in the field of MEMS. The bistability in these membranes is caused by an in-plane stress, which is often induced during fabrication. If this stress exceeds a critical value it causes the membrane to buckle, giving it two stable static deflection states. When exciting the integrated piezoelectric transducer it is possible to change the stress in the membrane, causing oscillations which can reach amplitudes high enough to make the membrane switch its deflection state. To make the high actuator deflections these devices exhibit usable, the nonlinear dynamics of the switching process need to be understood. Therefore, a mathematical model based on the von Karman plate equation is implemented in this work. Using Galerkin's method the deflection of the plate is approximated by a superposition of a finite number of its vibrational eigenmodes. This reduces the problem to a set of coupled nonlinear ordinary differential equations. Each equation represents the equation of motion for one of the considered modes. Approximate solutions for this system are acquired using numerical integration. A four mode model for a plate with typical dimensions for bistable MEMS devices is studied in order to gain information on the system dynamics. This work finds a high influence of the pre-stress applied during fabrication on the plate dynamics. While a higher pre-stress increases the static membrane deflection, which is beneficial for the use as an actuator, it also leads to complex multi-modal dynamics, which should be avoided. Further attention is paid on the influence of the excitation signal on the dynamics during switching. Using a finite pulse train to excite oscillations can lead to increased control over the number of switching events excited. We find that while a small number of pulses leads to dynamics that are easier to control, more pulses lower the excitation amplitudes needed in order to induce switching.

Contents

Kurzfassung	iv
Abstract	v
Contents	vi
1 Introduction	1
2 Related Works	3
3 Background Knowledge	5
3.1 Piezoelectric Bistable MEMS Membranes	5
3.2 Parametric Resonance	7
3.3 Elastic Material Properties	8
3.4 Von Karman Plate Theory	10
3.5 Galerkin's Method	16
4 Mathematical Model	18
4.1 Galerkin Solution of the Airy Function	21
4.2 Galerkin Solution of the von Karman Equation	23
4.3 Critical Stress	25
4.4 Elastic Potential Energy	27
5 Comparison of Numerical Integration Algorithms	29
6 Simulation Results	35
6.1 Static Analysis	36
6.2 Initiation of Snap-through	38

7 Conclusion and Future Work	57
A ODE coefficients	59
List of Figures	60
List of Tables	62
Bibliography	63

List of Abbreviations

DEQ Differential Equation.

FEM Finite Element Method.

IOT Internet of Things.

LiDAR Light Detection and Ranging.

MEMS Micro-Electro-Mechanical Systems.

ODE Ordinary Differential Equation.

Chapter 1

Introduction

Unseen by the average consumer, MEMS (Micro-Electro-Mechanical Systems) have widespread uses in our lives, with applications ranging from consumer goods to automotive, medical, IOT and many others. These devices, with typical dimensions from several hundreds of nanometers to a few millimeters are usually fabricated using semiconductor fabrication technology. Compatibility of a structure's design with standard fabrication procedures often decides over the economic success of these devices. MEMS devices can be broadly categorized as sensors or actuators. An example for the former would be MEMS accelerometers used in smartphones and airbags. Applications for MEMS actuators include inkjet printers, micro-pumps or micro-mirrors, which are used in LiDAR systems [8][10][14]. A common limitation of MEMS actuators is their low deflection, typically in the nanometer regime, especially when operated out of resonance. Bistable MEMS offer a way to overcome this limitation. These devices are defined by having two stable static ground states instead of one and can exhibit static deflections up to the ten micrometer regime. Bistable MEMS can be implemented by applying mechanical in-plane stress to thin beams or plates. If this pre-stress exceeds the critical stress the structure will buckle, leaving it with two stable static configurations. In order to use these bistable structures as an actuator, a method of switching between these ground states has to be implemented. Recently, the use of piezoelectric thin films has been proposed both for inducing pre-stress as well as for forming an integrated transducer element to stimulate actuation [3][4][5]. By applying voltage pulses to the piezoelectric actuator the mechanical stress in the membrane is changed. This periodic change in stress can be used to excite oscillations of the membrane in one of the ground states.

Large enough oscillation amplitudes will cause the membrane to snap through from one static buckling ground state to the other. Experimental data on the actuation of these bistable MEMS membranes show complex nonlinear switching behavior with multiple modes of vibration participating in the snap-through process. For the use of these devices as actuators, reliable and energy efficient switching is needed. Therefore, a thorough understanding of the dynamics at play is of interest.

This work introduces a mathematical framework describing the dynamics of thin parametrically excited buckled plates. The plates are assumed to be of rectangular geometry and made of an isotropic, homogeneous material. Using the von Karman plate equation and Galerkin's method the plates out-of-plane deflection is described by a system of coupled nonlinear differential equations. Each differential equation is the equation of motion for one vibrational mode of the plate. With this discretization approach, the plate motion is approximated as the linear superposition of the dynamics of all considered modes. The described approach is adaptable to any number of vibrational modes.

In order to gain an understanding of the dynamics at play and the impact of design choices, simulation data for a micro plate are gathered. For this study, a four mode model for a square plate of dimensions typical for bistable MEMS membranes is analysed. Investigations on the influence of the mechanical pre-stress and different methods of excitation are performed. The pre-stress is an important parameter directly influencing the static buckling deflection of the actuator. However, there is no sufficient understanding of its influence on the snap-through dynamics. To enable reliable, efficient actuation the space of excitation parameters is investigated for different membrane configurations.

Chapter 2

Related Works

In the existing experimental studies on piezoelectric bistable MEMS membranes Dorfmeister et al. [4] describe an efficient way of inducing snap-through. A piezoelectric transducer with two contacting electrodes covering the membrane surface makes it possible to vary the mechanical stress in the membrane. By applying a series of voltage pulses parametric resonance can be used to excite oscillations, which can cause the membrane to switch from one ground state to the other. This snap-through process enables power efficient switching between the equilibrium states. The observed dynamics during snap-through are highly nonlinear and can be both uni-modal and multi-modal, depending on the electrode design [5].

For a more thorough understanding of the observed dynamics a theoretical model is needed that describes the system dynamics and inter-mode coupling during the switching process of these devices. The displacement of MEMS structures is often modeled as infinitesimally small in order to use a simplified linearized model of the dynamics at play. This assumption, however, does not hold for buckled structures since they can display displacement in the same order of magnitude as their thickness or even above. We therefore look at existing literature describing buckling and snap-through phenomena. A wealth of work studying one-dimensional buckled beams is available. Chandra et al. [1] describe snap-through in shallow arches under out-of-plane forcing. A single-degree of freedom model, as well as a FEM model were implemented and the boundaries of snap-through in the forcing parameter space were studied. The results show, that the FEM model predicts snap-through for more sets of forcing parameters than the single-degree of freedom

model. This indicates, that the single-degree of freedom model can not sufficiently describe the system dynamics and a more detailed model is needed. Emam and Abdalla [6] study parametric resonance in simply supported buckled beams under in-plane excitation. The Galerkin approach is used to obtain a reduced order model of the governing equation. This study finds no influence of the second, or higher order modes on the dynamics of the system. Ilanko describes a model for simply supported rectangular plates with in-plane loading. By using the Galerkin approach the von Karman differential equation is reduced to a finite set of N single-degree of freedom differential equations representing N different modes of vibration. By numerically solving this set of equations the natural frequencies of plates can be calculated. The study shows, that the natural frequencies calculated with a four term solution significantly differ from those of the one-term solution. However, a solution including nine terms does not significantly change the results anymore [7]. Similarly Murphy and Virgin use Galerkin's method to solve the Airy function as well as the von Karman equation for clamped rectangular plates. They further study the temperature dependency of the small amplitude natural frequencies of these plates [9]. Since most of the existing studies on buckled plates are concerned with the stability of macroscopic mechanical structures most of them focus on small amplitude vibrations in order to predict when structures will fail. However, for bistable MEMS membranes snap-through is not a worst-case scenario that has to be avoided, but rather the standard mode of operation. Therefore we aim to understand the dynamics of snap-through and also snap-back movements.

Chapter 3

Background Knowledge

3.1 Piezoelectric Bistable MEMS Membranes

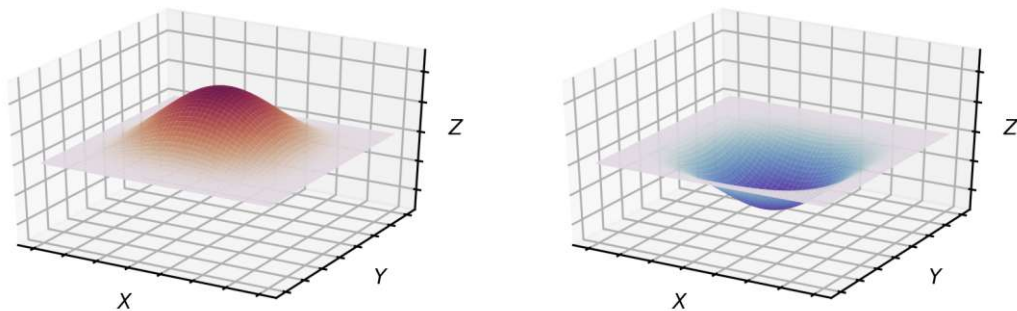


Figure 3.1: Stable ground states of a bistable MEMS membrane. Left image: buckled up, right image: buckled down

The motivation for this thesis is based on previous work performed at the Institute of Sensor and Actuator Systems at the TU Wien on bistable MEMS membranes which are actuated by a piezoelectric transducer. During fabrication of these membranes considerable compressive in-plane stress is induced. If this stress exceeds a critical value σ_c the membrane buckles. This means the membrane now has two stable ground-states that can be held without introducing additional energy. Figure 3.1) shows the two possible buckling states, buckled upwards and downwards. Switching between these two stable states is made possible by a piezoelectric transducer, which consists of an aluminum nitride (AlN) layer covering the surface of the

membrane. This piezo-layer is contacted by electrode layers on either side. The transition between the ground states is a highly non-linear process. A typical membrane material stack consists of a $2\ \mu\text{m}$ silicon device layer, an $800\ \text{nm}$ SiN_x layer, a $250\ \text{nm}$ SiO_2 layer, and a $400\ \text{nm}$ AlN layer sandwiched between $200\ \text{nm}$ top and bottom Cr/Au electrodes resulting in a $3.13\ \mu\text{m}$ thick membrane (figure 3.2) [4].

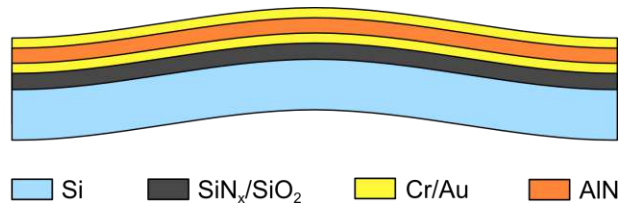


Figure 3.2: Membrane material stack bottom to top: $2\ \mu\text{m}$ Si, $800\ \text{nm}$ SiN_x , $250\ \text{nm}$ SiO_2 , $200\ \text{nm}$ Cr/Au , $400\ \text{nm}$ AlN , $200\ \text{nm}$ Cr/Au

The aluminum nitride layer introduces both, the static pre-stress from the fabrication process as well as the variable piezo-stress used to actuate the membrane. The piezo-stress is created by the inverse piezoelectric effect. The piezoelectric effect describes the generation of electric charge due to mechanical stress in specific materials. This effect requires the material to have a crystalline structure with no inversion symmetry. For the use in actuators it is convenient that the piezoelectric effect is reversible, meaning that a mechanical stress can be created by applying an electric field. In order to switch the membrane state a series of voltage pulses is applied to the piezo-layer at a specific resonance frequency. The periodic change of the in-plane stress acts as a parametric excitation inducing oscillations of the membranes deflection. If these oscillations reach a sufficient amplitude the membrane can snap-through from its current state to the opposite stable state. Depending on the amplitude and frequency of the excitation signal the membrane can switch its state multiple times. After the excitation period the oscillations die out and the membrane remains in one of its stable configurations. This feature is preferred for a desirable actuator, since the membrane only needs energy to switch between ground states. A second benefit are the high buckling deflections of these devices in comparison to state of the art MEMS actuators [3] [4].

3.2 Parametric Resonance

Parametric resonance is a phenomenon that can appear when an oscillator is driven by a periodic change in one or more of its parameters [11]. For a mechanical oscillator this parameter can for example be the oscillator's spring constant or its mass. In the piezoelectric bistable MEMS membranes described in section 3.1 we speak of parametric excitation, since the oscillations in the membrane are excited by changing the mechanical stress of the system. We will see in section 4.4 that this effectively changes the stiffness of the system. An equation that describes many parametrically driven systems is the Mathieu equation (3.1)

$$\ddot{\theta} + d\dot{\theta} + \omega_0^2(1 + f \cos(\omega t))\theta = 0 \quad (3.1)$$

with the parametric drive $f \cos(\omega t)$, the damping ratio d and the natural frequency ω_0 . In a mechanical system, the state variable θ usually represents a displacement or angle. Comparing the natural frequency term in the Mathieu equation (3.1) to the one in the harmonic oscillator (3.3) we notice that in the Mathieu equation the natural frequency is not a constant. Instead the natural frequency varies periodically with ω . For a specific choice of the parameters f and ω the oscillation amplitude in this systems will grow exponentially without any bounds. This phenomenon is called parametric resonance and occurs for

$$\omega_n = 2\omega_0/n, \quad n = 1, 2, 3, \dots \quad (3.2)$$

At these frequencies ω_n the equilibrium point $(\theta, \dot{\theta}) = (0, 0)$ becomes unstable and the oscillations grow with time. The strongest oscillations will be excited for $\omega = 2\omega_0$. Parametric resonance causes an exponential growth in oscillations over time. This is best shown when comparing the system in (3.1) to a simple harmonic oscillator (3.3).

$$\ddot{\theta} + d\dot{\theta} + \omega_0^2\theta = f \cos(\omega t) \quad (3.3)$$

Figure 3.3 shows the growth of the state variable θ for a parametrically excited system (left) compared to a harmonic oscillation (right). While for the case of a

harmonic oscillator driven by an external force the state variable slowly rises to a maximum level, the oscillations of the parametrically driven system are unbounded. The Mathieu equation is not solvable analytically, which is why these results are acquired by using a numerical solver.

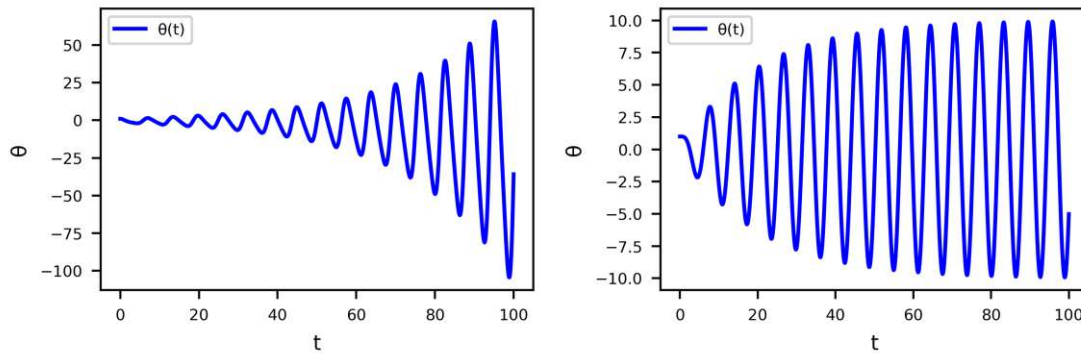


Figure 3.3: Comparison between the response of a parametric (left) and a harmonic (right) oscillator. The parameters for this simulation were $d = 0.1$, $\omega = 1$, $\omega_0 = 1$, $f = 1$, $(\theta, \dot{\theta}) = (1, 0)$

3.3 Elastic Material Properties

In order to describe the behavior of the studied membranes we need to understand the concept of mechanical stresses and strains. It should be noted, that this will be a simplified description, tailored to the scope of this work. Mechanical stress is a measure of force per area defined at a point. For a surface A with a uniform force F acting along its surface normal we can write $\sigma = F/A$. We can differentiate stresses into normal stresses σ_n and shear stresses τ_{nm} . For normal stresses the direction of the force and the normal vector of the surface it acts upon are the same, while for shear stresses they are perpendicular. For shear stresses the first index describes the direction of the surface normal and the second index the direction of the force. Figure 3.4 illustrates the stress components for a cube of infinitesimal dimensions.

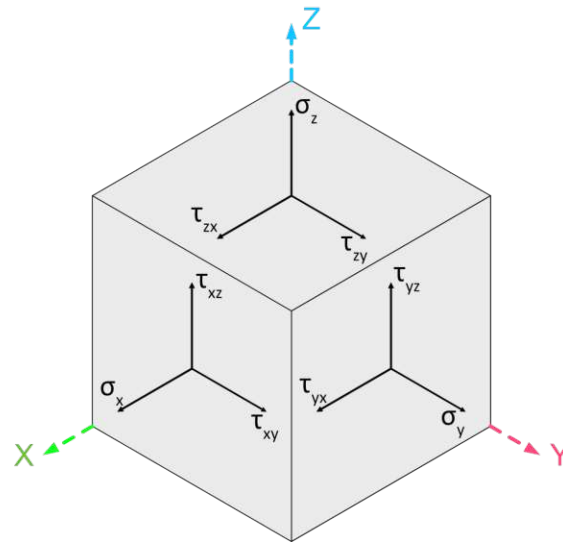


Figure 3.4: Stress components σ_i and τ_{ij} acting on an infinitesimal cube

The mechanical strain represents the relative deformation of a material due to stress. A simple example of this would be a string of length L with a force applied to both ends stretching it by a deformation δ (figure 3.5). The strain for this string is $\varepsilon = \delta/L$.

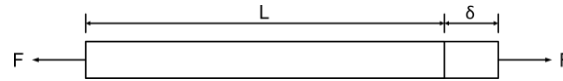


Figure 3.5: One-dimensional strain sketch

Mechanical strains can again be separated into normal strains ε_n and shear strains γ_{nm} . Assuming linear elastic material properties we can relate the stresses and strains using the Young's modulus

$$E = \frac{\sigma_n}{\varepsilon_n} \quad (3.4)$$

It should be noted, that the description of the Young's modulus as a constant is only correct for isotropic materials. For non-isotropic materials the Young's modulus takes the form of a 4-th order tensor with 36 components. Equation (3.4) does not take the Poisson effect into account. This effect tells us that a material that is stretched along an axis n experiences compression along a perpendicular

axis m . To mathematically describe this effect we use Poisson's ratio ν (3.5).

$$\varepsilon_m = -\nu\varepsilon_n \quad (3.5)$$

This leads us to the relations between normal strain and stress in an isotropic material.

$$\begin{aligned} \varepsilon_x &= \frac{1}{E} [\sigma_x - \nu(\sigma_y + \sigma_z)] \\ \varepsilon_y &= \frac{1}{E} [\sigma_y - \nu(\sigma_x + \sigma_z)] \\ \varepsilon_z &= \frac{1}{E} [\sigma_z - \nu(\sigma_x + \sigma_y)] \end{aligned} \quad (3.6)$$

What we are missing is the relationship between shear strains and stresses, which are connected with the shear modulus G

$$G = \frac{E}{2(1 + \nu)}. \quad (3.7)$$

In an isotropic material the shear strains are related to the shear stresses by

$$\begin{aligned} \gamma_{xy} &= \frac{1}{G} \tau_{xy} \\ \gamma_{xz} &= \frac{1}{G} \tau_{xz} \\ \gamma_{yz} &= \frac{1}{G} \tau_{yz}. \end{aligned} \quad (3.8)$$

3.4 Von Karman Plate Theory

The mathematical framework used to describe the MEMS membranes studied in this thesis will be von Karman's thin plate theory. Strictly speaking the term membrane is not correct for the devices described. In classical theory, membranes do not possess any bending stiffness. Measurements by Dorfmeister [3] show that the studied bistable MEMS membranes show pure thin plate behavior. In this work both terms will be used interchangeably. When using the term membranes we refer to thick membranes that exhibit plate behavior. Figure 3.6 shows the described

plates with planar dimensions L_x and L_y in x and y direction and a thickness h in z direction. To describe the behavior of thin plates under deformation we use the Kirchhoff hypothesis, which consists of three assumptions:

1. Straight lines perpendicular to the midsurface remain straight after deformation
2. Straight lines perpendicular to the midsurface rotate such that they remain perpendicular to the midsurface after deformation
3. The thickness of the plate does not change (or: straight lines perpendicular to the midsurface do not experience elongation)

The plate displacements (u, v, w) in (x, y, z) directions can be written as

$$u = \bar{u} - z \frac{\partial w}{\partial x}, \quad v = \bar{v} - z \frac{\partial w}{\partial y}, \quad w = \bar{w} \quad (3.9)$$

where the overline indicates the location of the midsurface.

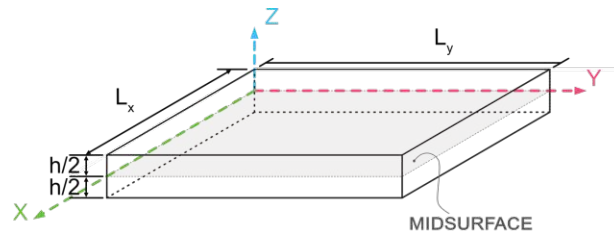


Figure 3.6: Rectangular plate geometry

The plate is under in-plane stress, no forces are applied in z -direction. According to the Kirchhoff hypothesis we neglect ε_z , γ_{xz} and γ_{yz} . The strains associated with

the deflections are

$$\begin{aligned}\varepsilon_x &= \frac{\partial u}{\partial x} + \frac{1}{2} \left(\frac{\partial w}{\partial x} \right)^2 \\ \varepsilon_y &= \frac{\partial v}{\partial y} + \frac{1}{2} \left(\frac{\partial w}{\partial y} \right)^2 \\ \gamma_{xy} &= \frac{\partial v}{\partial x} + \frac{\partial u}{\partial y} + \frac{\partial w}{\partial x} \frac{\partial w}{\partial y}.\end{aligned}\tag{3.10}$$

For each of these strains the last term is a retained non-linearity from the non-linear Euler-Lagrange strain tensor. In MEMS devices, this non-linear description of the strains is usually not required, due to the infinitesimally small displacements and strains. However, since our plate model permits finite displacements w we need to consider some non-linearity. For a more thorough coverage of the Euler-Lagrange strain tensor and the terms that need to be considered in the theory of thin plates, we refer to [12]. Using (3.9), we can write the strains as a function of the midsurface deflection as

$$\begin{aligned}\varepsilon_x &= \frac{\partial \bar{u}}{\partial x} + \frac{1}{2} \left(\frac{\partial w}{\partial x} \right)^2 - z \frac{\partial^2 w}{\partial x^2} \\ \varepsilon_y &= \frac{\partial \bar{v}}{\partial y} + \frac{1}{2} \left(\frac{\partial w}{\partial y} \right)^2 - z \frac{\partial^2 w}{\partial y^2} \\ \gamma_{xy} &= \frac{\partial \bar{v}}{\partial x} + \frac{\partial \bar{u}}{\partial y} + \frac{\partial w}{\partial x} \frac{\partial w}{\partial y} - 2z \frac{\partial^2 w}{\partial x \partial y}.\end{aligned}\tag{3.11}$$

These strain-displacement relations called the von Karman strains will build the foundation to gather the equations of motion for our plate. We will use the principle of virtual displacements and Hamilton's principle to derive the equations of motion. For a deeper study of the underlying theory please refer to [12] and [13] We can state Hamilton's principle as

$$\delta \int_{t_1}^{t_2} [T - (U + V)] dt = 0\tag{3.12}$$

where U is the strain energy, V the work done by applied forces and T is the kinetic

energy. At this point we can assume that there are no externally applied loads. The virtual strain energy δU for a linear elastic material is

$$\begin{aligned}\delta U &= \int_V \sigma_{ij} \delta \varepsilon_{ij} dV \\ \delta U &= \int_0^{L_y} \int_0^{L_x} \int_{-\frac{h}{2}}^{\frac{h}{2}} \sigma_x \delta \varepsilon_x + \sigma_y \delta \varepsilon_y + \tau_{xy} \delta \gamma_{xy} dz dx dy.\end{aligned}\tag{3.13}$$

Using (3.11) we can write the virtual strains as

$$\begin{aligned}\delta \varepsilon_x &= \frac{\partial \delta \bar{u}}{\partial x} + \frac{\partial w}{\partial x} \frac{\partial \delta w}{\partial x} - z \frac{\partial^2 \delta w}{\partial x^2} \\ \delta \varepsilon_y &= \frac{\partial \delta \bar{v}}{\partial y} + \frac{\partial w}{\partial y} \frac{\partial \delta w}{\partial y} - z \frac{\partial^2 \delta w}{\partial y^2} \\ \delta \gamma_{xy} &= \frac{\partial \delta \bar{v}}{\partial x} + \frac{\partial \delta \bar{u}}{\partial y} + \frac{\partial \delta w}{\partial x} \frac{\partial w}{\partial y} + \frac{\partial w}{\partial x} \frac{\partial \delta w}{\partial y} - 2z \frac{\partial^2 \delta w}{\partial x \partial y}.\end{aligned}\tag{3.14}$$

Integrating the stresses over the plate thickness gives us the so called stress resultants N (thickness integrated forces) and M (thickness integrated moments). Figures 3.7 and 3.8 illustrate these stress resultants on a plate element.

$$N_x = \int_{-\frac{h}{2}}^{\frac{h}{2}} \sigma_x dz, \quad N_y = \int_{-\frac{h}{2}}^{\frac{h}{2}} \sigma_y dz, \quad N_{xy} = \int_{-\frac{h}{2}}^{\frac{h}{2}} \tau_{xy} dz\tag{3.15}$$

$$M_x = \int_{-\frac{h}{2}}^{\frac{h}{2}} \sigma_x z dz, \quad M_y = \int_{-\frac{h}{2}}^{\frac{h}{2}} \sigma_y z dz, \quad M_{xy} = \int_{-\frac{h}{2}}^{\frac{h}{2}} \tau_{xy} z dz\tag{3.16}$$

Plugging (3.14), (3.15) and (3.16) into (3.13) and integrating by parts in order to

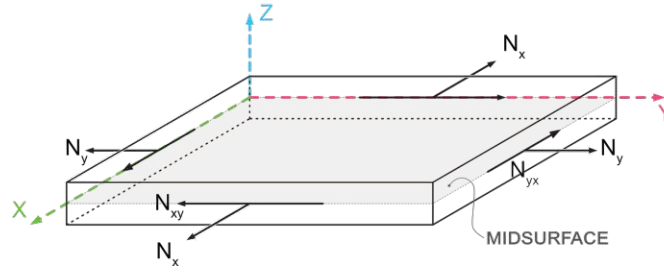


Figure 3.7: Thickness integrated forces of a rectangular plate

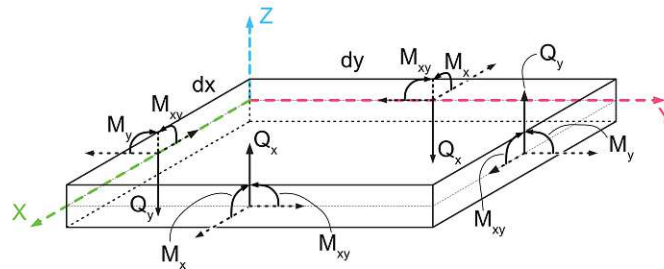


Figure 3.8: Shear forces and thickness integrated moments of a rectangular plate

separate the δ operator from the differentiations we get

$$\begin{aligned}
 \delta U = & - \int_0^{L_y} \int_0^{L_x} \delta \bar{u} \left(\frac{\partial N_x}{\partial x} + \frac{\partial N_{xy}}{\partial y} \right) + \delta \bar{v} \left(\frac{\partial N_y}{\partial y} + \frac{\partial N_{xy}}{\partial x} \right) \\
 & + \delta \bar{w} \left[\left(\frac{\partial N_x}{\partial x} + \frac{\partial N_{xy}}{\partial y} \right) \frac{\partial w}{\partial x} + \left(\frac{\partial N_y}{\partial y} + \frac{\partial N_{xy}}{\partial x} \right) \frac{\partial w}{\partial y} \right. \\
 & \left. + N_x \frac{\partial^2 w}{\partial x^2} + N_y \frac{\partial^2 w}{\partial y^2} + 2N_{xy} \frac{\partial^2 w}{\partial x \partial y} + \frac{\partial^2 M_x}{\partial x^2} + \frac{\partial^2 M_y}{\partial y^2} + 2 \frac{\partial^2 M_{xy}}{\partial x \partial y} \right] dx dy.
 \end{aligned} \tag{3.17}$$

The virtual kinetic energy δT for our plate is

$$\delta T = \int_0^{L_y} \int_0^{L_x} \int_{-\frac{h}{2}}^{\frac{h}{2}} \rho \left(\frac{\partial \bar{u}}{\partial t} \frac{\partial \delta \bar{u}}{\partial t} + \frac{\partial \bar{v}}{\partial t} \frac{\partial \delta \bar{v}}{\partial t} + \frac{\partial w}{\partial t} \frac{\partial \delta w}{\partial t} \right) dz dx dy \tag{3.18}$$

which by again utilizing integration by parts becomes

$$\delta T = - \int_0^{L_y} \int_0^{L_x} \mu \left(\frac{\partial^2 \bar{u}}{\partial t^2} \delta \bar{u} + \frac{\partial^2 \bar{v}}{\partial t^2} \delta \bar{v} + \frac{\partial^2 w}{\partial t^2} \delta w \right) dx dy \tag{3.19}$$

with the areal mass density $\mu = \rho h$. With these expressions for the virtual kinetic and strain energy we can rewrite Hamiltons principle as

$$\begin{aligned}
 0 = & \int_{t_1}^{t_2} \int_0^{L_y} \int_0^{L_x} \delta \bar{u} \left(\frac{\partial N_x}{\partial x} + \frac{\partial N_{xy}}{\partial y} - \mu \frac{\partial^2 \bar{u}}{\partial t^2} \right) \\
 & + \delta \bar{v} \left(\frac{\partial N_y}{\partial y} + \frac{\partial N_{xy}}{\partial x} - \mu \frac{\partial^2 \bar{v}}{\partial t^2} \right) + \delta w \left[\left(\frac{\partial N_x}{\partial x} + \frac{\partial N_{xy}}{\partial y} \right) \frac{\partial w}{\partial x} \right. \\
 & + \left(\frac{\partial N_y}{\partial y} + \frac{\partial N_{xy}}{\partial x} \right) \frac{\partial w}{\partial y} + N_x \frac{\partial^2 w}{\partial x^2} + N_y \frac{\partial^2 w}{\partial y^2} + 2N_{xy} \frac{\partial^2 w}{\partial x \partial y} \\
 & \left. + \frac{\partial^2 M_x}{\partial x^2} + \frac{\partial^2 M_y}{\partial y^2} + 2 \frac{\partial^2 M_{xy}}{\partial x \partial y} - \mu \frac{\partial^2 w}{\partial t^2} \right] dx dy dt
 \end{aligned} \tag{3.20}$$

This statement can only be true for all times if the coefficients of $\delta \bar{u}, \delta \bar{v}$ and δw are equal zero. The equation of motion for the plate deflection w therefore is

$$\begin{aligned}
 & N_x \frac{\partial^2 w}{\partial x^2} + N_y \frac{\partial^2 w}{\partial y^2} + 2N_{xy} \frac{\partial^2 w}{\partial x \partial y} \\
 & + \frac{\partial^2 M_x}{\partial x^2} + \frac{\partial^2 M_y}{\partial y^2} + 2 \frac{\partial^2 M_{xy}}{\partial x \partial y} - \mu \frac{\partial^2 w}{\partial t^2} = 0.
 \end{aligned} \tag{3.21}$$

We want our equation to describe the deflection w of the plate in relation to the stress resultant N . Therefore we need to rewrite the terms containing the thickness integrated moments M . From the relations between strain and stress in (3.6) and (3.8) we can write the in-plane stresses for our thin plates as

$$\begin{aligned}
 \sigma_x &= \frac{E}{1 - \nu^2} (\varepsilon_x + \nu \varepsilon_y) \\
 \sigma_y &= \frac{E}{1 - \nu^2} (\varepsilon_y + \nu \varepsilon_x) \\
 \tau_{xy} &= G \gamma_{xy}.
 \end{aligned} \tag{3.22}$$

With these in-plane stresses and the expressions for the strains in (3.11) we can

evaluate the thickness integrated moments M from (3.16) as

$$\begin{aligned} M_x &= -D \left(\frac{\partial^2 w}{\partial x^2} + \nu \frac{\partial^2 w}{\partial y^2} \right) \\ M_y &= -D \left(\frac{\partial^2 w}{\partial y^2} + \nu \frac{\partial^2 w}{\partial x^2} \right) \\ M_{xy} &= -D(1 - \nu) \frac{\partial^2 w}{\partial x \partial y} \end{aligned} \quad (3.23)$$

with the flexural rigidity $D = Eh^3/[12(1 - \nu^2)]$. Using these expressions and adding a linear damping term with a damping coefficient κ we rewrite (3.21) as

$$\mu \frac{\partial^2 w}{\partial t^2} + \kappa \frac{\partial w}{\partial t} + D \nabla^4 w = N_x \frac{\partial^2 w}{\partial x^2} + N_y \frac{\partial^2 w}{\partial y^2} + 2N_{xy} \frac{\partial^2 w}{\partial x \partial y} \quad (3.24)$$

with the biharmonic operator

$$\nabla^4 = \frac{\partial^4}{\partial x^4} + \frac{\partial^4}{\partial y^4} + 2 \frac{\partial^4}{\partial x^2 \partial y^2}. \quad (3.25)$$

This is the von Karman nonlinear partial differential equation, which will be used to describe the dynamic behavior of the membranes studied in this work. Equation 3.20 would also give us the equations of motion for the deflections u and v .

3.5 Galerkin's Method

The Galerkin method is an approach to acquire approximate results for distributed parameter systems which include, but are not limited to partial differential equations. It is based on the method of weighted residuals. With a linear differential operator \mathcal{L} we write the operator equation

$$\mathcal{L}[w(\mathbf{x}, t)] = 0 \quad (3.26)$$

with the homogeneous boundary conditions

$$\mathcal{B}_\mu[w(\mathbf{x}, t)] = 0, \quad \mu = 1, 2, \dots, p \quad (3.27)$$

for a differential expression of the order $2p$ [13]. We assume the solution to be a superposition of approximation functions ϕ_j

$$w(\mathbf{x}, t) = \sum_{j=1}^N q_j(t) \phi_j(\mathbf{x}) \quad (3.28)$$

with time dependant generalized coordinates $q_j(t)$. These functions ϕ_j need to fulfill three requirements:

1. Continuity: The functions need to be differentiable of the same order as the order of the differential equation.
2. Boundary Conditions: The functions need to fulfill all boundary conditions \mathcal{B}_μ .
3. Orthogonality: $\{\phi_j\}$ needs to be a set of orthogonal functions.

Since we would need an infinite set of functions to represent every possible solution, but only use a set of N functions our approximation can have a non-zero residual R_N

$$R_N = \mathcal{L} \left(\sum_{j=1}^N q_j(t) \phi_j(\mathbf{x}) \right) \neq 0. \quad (3.29)$$

We require this residual to be orthogonal to our set of chosen approximation functions in order to determine the generalized coordinates q_i . By multiplying the residual R_N with each of our basis functions and integrating over the domain Ω we acquire a set of N differential equations for the generalized coordinates $q_i(t)$.

$$\int_{\Omega} \phi_i \mathcal{L} \left(\sum_{j=1}^N q_j(t) \phi_j(\mathbf{x}) \right) d\mathbf{x} = 0 \quad (3.30)$$

Chapter 4

Mathematical Model

As described in section 3.4 we use von Karman's Plate theory and the Kirchoff hypothesis to describe thin rectangular microplates of planar dimensions L_x and L_y with a height h . Additionally the plate is clamped along its edges to the rest of the silicon wafer. The aim of this work is to understand the general dynamics which are to be expected of axially loaded thin plates. In order to use the theory described in 3.3 and 3.4 we assume the plate to be made of a homogeneous linear elastic material with stress strain relations as described in (3.6) and (3.8). This means we neglect the exact structure of the material stack described in section 3.1. Furthermore we will neglect the anisotropy of silicon and assume the plate to be made of an isotropic material. We also simplify the physical mechanisms that lead to damping and model all damping as local viscous damping. In MEMS displacements are often assumed to be infinitesimally small. However for buckled plates this assumption is not valid, since the displacement $w(x, y, t)$ in z-direction is not negligible in comparison to the plate thickness h . Because of the clamped boundary conditions we assume this displacement w to describe all deformations of the plate due to bending, neglecting the displacements in x- and y-direction. However we still need to take in-plane stresses into account, since the geometric nonlinearity caused by the deflection w causes coupling of in-plane stresses to bending moments. We already know from section 3.1 that our plates are under two sources of in-plane stress. The constant pre-stress which is induced during fabrication, and the variable piezo-stress. As established in (3.15) we describe the stress in terms of the thickness integrated stress resultants N . We can now

decompose each stress resultant into its three components.

$$N_\mu(t, x, y) = N_\mu^{(b)}(t, x, y) + N_\mu^{(0)}(x, y) + N_\mu^{(p)}(t, x, y), \quad \mu \in \{x, y, xy\}. \quad (4.1)$$

We model the initial pre-stress $N_\mu^{(0)}$ and the piezo-stress $N_\mu^{(p)}$ to be constant over the whole plate. $N_\mu^{(b)}$, the in-plane stress due to bending of the plate however is position dependant. We also assume that the pre- and piezo-stress do not have a shear component.

$$N_{xy}^{(0)}(x, y) = N_{xy}^{(p)}(t, x, y) = 0. \quad (4.2)$$

We now have two unknowns in the von Karman equation. The plate displacement w , and the in-plane stress resultants N_x , N_y and N_{xy} . In the von Karman plate equation the stress resultants are expressed in terms of the Airy stress function F , which is defined as

$$\frac{\partial^2 F}{\partial x^2} = N_y, \quad \frac{\partial^2 F}{\partial y^2} = N_x, \quad \frac{\partial^2 F}{\partial x \partial y} = -N_{xy}. \quad (4.3)$$

Using the Airy function F we rewrite the von Karman equation (3.24) as

$$\mu \frac{\partial^2 w}{\partial t^2} + \kappa \frac{\partial w}{\partial t} + D \nabla^4 w = \frac{\partial^2 F}{\partial y^2} \frac{\partial^2 w}{\partial x^2} + \frac{\partial^2 F}{\partial x^2} \frac{\partial^2 w}{\partial y^2} - 2 \frac{\partial^2 F}{\partial x \partial y} \frac{\partial^2 w}{\partial x \partial y}. \quad (4.4)$$

The interplay between in-plane stresses and the plate displacement in z-direction is expressed in the compatibility equation

$$\nabla^4 F = Eh \left[\left(\frac{\partial^2 w}{\partial x \partial y} \right)^2 - \frac{\partial^2 w}{\partial x^2} \frac{\partial^2 w}{\partial y^2} \right] \quad (4.5)$$

. Equations (4.4) and (4.5) form a system of two nonlinear fourth order partial differential equations, which have to be solved together in order to derive the motion of the plate.

Since we know of no analytic solutions to the set of von Karman equations we

use the Galerkin approach described in 3.5 to obtain an approximate solution. With this method the deflection $w(x, y, t)$ is approximated by a superposition of N orthogonal basis functions

$$w(x, y, t) \approx \sum_{j=1}^N q_j(t) \phi_j(x, y). \quad (4.6)$$

This divides the solution into the spatial basis functions ϕ_j and the time-dependant generalized coordinates q_j . The basis functions, also called mode shapes, need to fulfill the boundary conditions for the clamped plate.

$$\begin{aligned} w(0, y) = w(L_x, y) = w(x, 0) = w(x, L_y) = 0, \\ \frac{\partial w}{\partial x}(0, y) = \frac{\partial w}{\partial x}(L_x, y) = \frac{\partial w}{\partial y}(x, 0) = \frac{\partial w}{\partial y}(x, L_y) = 0 \end{aligned} \quad (4.7)$$

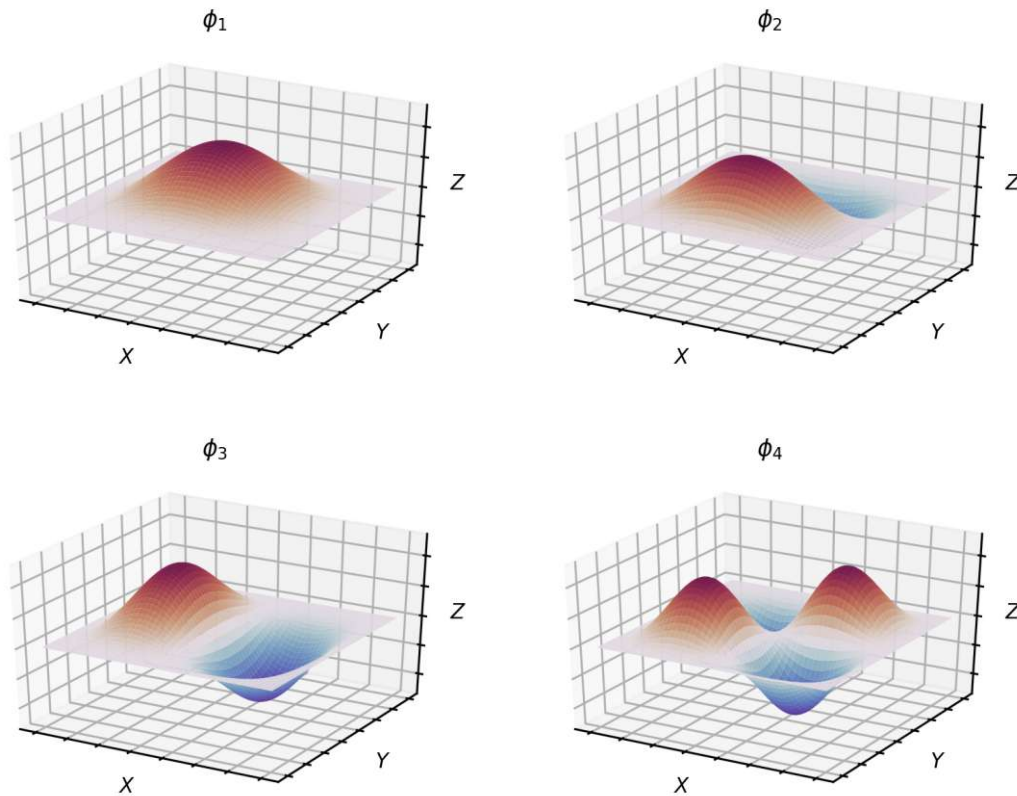
The basis functions also resemble the free vibrational modes for a clamped rectangular plate. We choose the following functions also employed by Murphy [9].

$$\begin{aligned} \phi_i(x, y) = & \left(\cos \left((i_x - 1) \frac{\pi x}{L_x} \right) - \cos \left((i_x + 1) \frac{\pi x}{L_x} \right) \right) \\ & \times \left(\cos \left((i_y - 1) \frac{\pi y}{L_y} \right) - \cos \left((i_y + 1) \frac{\pi y}{L_y} \right) \right) \end{aligned} \quad (4.8)$$

with

$$i_x = \left\lfloor \frac{i + 1}{N/2} \right\rfloor, \quad i_y = i \pmod{N/2}. \quad (4.9)$$

Figure 4.1 shows the first four vibrational eigenmodes that are described by (4.8).

Figure 4.1: Mode shapes ϕ_1 , ϕ_2 , ϕ_3 and ϕ_4 for a clamped rectangular plate

4.1 Galerkin Solution of the Airy Function

The first step to solve the given system of differential equations is to find an expression for the unknown Airy function F by solving (4.5). Since this differential equation has the non-homogeneous boundary conditions

$$\begin{aligned} \frac{\partial^2 F}{\partial x^2}(x, 0) &= \frac{\partial^2 F}{\partial x^2}(x, L_y) = N_y \\ \frac{\partial^2 F}{\partial y^2}(0, y) &= \frac{\partial^2 F}{\partial y^2}(L_x, y) = N_x \end{aligned} \quad (4.10)$$

we need to split the solution into an external part $F^{(e)}$ which accounts for the initial pre-stress and the piezo-stress and an inhomogenous part $F^{(c)}$ which satisfies

the compatibility equation. For $F^{(e)}$ we will use the solution

$$F^{(e)} = \frac{1}{2}(x^2 N_x + y^2 N_y) \quad (4.11)$$

Gaining a suitable solution for $F^{(c)}$ is possible by using Galerkin's method. We first plug our expression for the approximated deflection $w(x, y, t)$ (4.6) into the compatibility equation (4.5).

$$\nabla^4 F^{(c)} = Eh \sum_{i=1}^N \sum_{j=1}^N q_i q_j \left[\frac{\partial^2 \phi_i}{\partial x \partial y} \frac{\partial^2 \phi_j}{\partial x \partial y} - \frac{\partial^2 \phi_i}{\partial x^2} \frac{\partial^2 \phi_j}{\partial y^2} \right] \quad (4.12)$$

We can now express $F^{(c)}$ in terms of the same basis functions ϕ_i used for the deflection w

$$F^{(c)} \approx \sum_{i=1}^N \sum_{j=1}^N \sum_{k=1}^N q_i(t) q_j(t) f_{ijk} \phi_k(x, y) \quad (4.13)$$

With (4.12) and (4.13) we get

$$\sum_{k=1}^N f_{ijk} \nabla^4 \phi_k = Eh \left[\frac{\partial^2 \phi_i}{\partial x \partial y} \frac{\partial^2 \phi_j}{\partial x \partial y} - \frac{\partial^2 \phi_i}{\partial x^2} \frac{\partial^2 \phi_j}{\partial y^2} \right] \quad (4.14)$$

Using Galerkin's approach we multiply by the approximation function ϕ_l and integrate over the domain $\Omega = [0, L_x] \times [0, L_y]$. This gives a set of algebraic equations for the coefficients f_{ijk} .

$$\sum_{k=1}^N f_{ijk} \left(F_{kl}^{(1)} + F_{kl}^{(2)} + 2F_{kl}^{(3)} \right) = Eh \left(F_{ijl}^{(4)} - F_{ijl}^{(5)} \right). \quad (4.15)$$

with

$$\begin{aligned}
 F_{kl}^{(1)} &= \int_{\Omega} \frac{\partial^4 \phi_k}{\partial x^4} \phi_l d\Omega, & F_{kl}^{(2)} &= \int_{\Omega} \frac{\partial^4 \phi_k}{\partial y^4} \phi_l d\Omega, & F_{kl}^{(3)} &= \int_{\Omega} \frac{\partial^4 \phi_k}{\partial x^2 \partial y^2} \phi_l d\Omega, \\
 F_{ijl}^{(4)} &= \int_{\Omega} \frac{\partial^2 \phi_i}{\partial x \partial y} \frac{\partial^2 \phi_j}{\partial x \partial y} \phi_l d\Omega, & F_{ijl}^{(5)} &= \int_{\Omega} \frac{\partial^2 \phi_i}{\partial x^2} \frac{\partial^2 \phi_j}{\partial y^2} \phi_l d\Omega.
 \end{aligned} \tag{4.16}$$

$F_{kl}^{(1)}$, $F_{kl}^{(2)}$ and $F_{kl}^{(3)}$ are diagonal matrices, which reduces (4.15) to

$$f_{ijk} \left(F_{kk}^{(1)} + F_{kk}^{(2)} + 2F_{kk}^{(3)} \right) = Eh \left(F_{ijk}^{(4)} - F_{ijk}^{(5)} \right). \tag{4.17}$$

The coefficients f_{ijk} can now easily be computed and plugged into (4.13) giving us the full Airy function.

$$F \approx F^{(e)} + F^{(c)} \tag{4.18}$$

4.2 Galerkin Solution of the von Karman Equation

With the solution for the Airy function we can use Galerkin's method in order to reduce the von Karman equation (4.4) to a set of N differential equations, one for each considered mode. In order to do this we substitute the approximated Airy function (4.18) and our approximation for the plate deflection (4.8) into (4.4).

$$\begin{aligned}
 0 &= \sum_{j=1}^N \left[\mu \frac{\partial^2 q_j}{\partial t^2} \phi_j + \kappa \frac{\partial q_j}{\partial t} \phi_j + D \left(\frac{\partial^4 \phi_j}{\partial x^4} + \frac{\partial^4 \phi_j}{\partial y^4} + 2 \frac{\partial^4 \phi_j}{\partial x^2 \partial y^2} \right) q_j - N_x \frac{\partial^2 \phi_j}{\partial x^2} q_j - \right. \\
 & \left. N_y \frac{\partial^2 \phi_j}{\partial y^2} q_j - \sum_{k=1}^N \sum_{l=1}^N \sum_{m=1}^N f_{jkm} \left(\frac{\partial^2 \phi_m}{\partial y^2} \frac{\partial^2 \phi_l}{\partial x^2} + \frac{\partial^2 \phi_m}{\partial x^2} \frac{\partial^2 \phi_l}{\partial y^2} - 2 \frac{\partial^2 \phi_m}{\partial x \partial y} \frac{\partial^2 \phi_l}{\partial x \partial y} \right) q_j q_k q_l \right]
 \end{aligned} \tag{4.19}$$

We again employ Galerkin's method by multiplying with the basis functions ϕ_i and integrating over the domain $\Omega = [0, L_x] \times [0, L_y]$. We now receive a system of N

nonlinear ordinary differential equations for the generalized coordinate functions q_i . Each equation takes the form

$$\mu M_{ij} \ddot{q}_j + \kappa M_{ij} \dot{q}_j + DK_{ij} q_j + N_x C_{ij}^{(x)} q_j + N_y C_{ij}^{(y)} q_j + G_{ijkl} q_j q_k q_l = 0 \quad (4.20)$$

M_{ij} is the mass matrix of the system and K_{ij} the stiffness matrix. We will call $C_{ij}^{(x)}$ and $C_{ij}^{(y)}$ the curvature matrices and G_{ijkl} the coupling matrix. The matrices are computed as

$$\begin{aligned} M_{ij} &= \int_{\Omega} \phi_i \phi_j d\Omega \\ K_{ij} &= \int_{\Omega} \phi_i \left(\frac{\partial^4 \phi_j}{\partial x^4} + \frac{\partial^4 \phi_j}{\partial y^4} + 2 \frac{\partial^4 \phi_j}{\partial x^2 \partial y^2} \right) d\Omega \\ C_{ij}^{(x)} &= - \int_{\Omega} \phi_i \frac{\partial^2 \phi_j}{\partial x^2} d\Omega \\ C_{ij}^{(y)} &= - \int_{\Omega} \phi_i \frac{\partial^2 \phi_j}{\partial y^2} d\Omega \\ G_{ijkl} &= -f_{jkm} \int_{\Omega} \phi_i \left(\frac{\partial^2 \phi_m}{\partial y^2} \frac{\partial^2 \phi_l}{\partial x^2} + \frac{\partial^2 \phi_m}{\partial x^2} \frac{\partial^2 \phi_l}{\partial y^2} - 2 \frac{\partial^2 \phi_m}{\partial x \partial y} \frac{\partial^2 \phi_l}{\partial x \partial y} \right) d\Omega \end{aligned} \quad (4.21)$$

Due to the orthogonality of the modes it is immediately visible that the mass matrix M_{ij} has to be diagonal. The stiffness and curvature matrices are diagonal as well. The diagonal curvature matrices statically shift the stiffness of the modes due to the initial pre-stress. They further modulate this stiffness in time due to the piezo-stress which acts as a parametric excitation on the system. Inspection of the coupling matrix G_{ijkl} reveals the inter-mode coupling can be described by three terms. We re-write (4.20) as

$$\mu M_{ij} \ddot{q}_j + \kappa M_{ij} \dot{q}_j + DK_{ij} q_j + N_x C_{ij}^{(x)} q_j + N_y C_{ij}^{(y)} q_j + G_{ij}^{(1)} q_j^3 + G_{ijk}^{(2)} q_j q_k^2 + G_{ijkl}^{(3)} q_j q_k q_l = 0 \quad (4.22)$$

This equation now contains three nonlinear coupling terms. These result from the coupling between the bending stress resultants and the bending moments included in the von Karman equation. The first of these terms contains the diagonal matrix $G_{ij}^{(1)}$. It describes the nonlinear Duffing-like self-coupling of each mode. In the coupling matrix $G_{ijk}^{(2)}$ only entries where $i = j$ are non-zero. The corresponding

term describes a nonlinear dispersive coupling of the current mode to any other mode. The last matrix is the $G_{ijkl}^{(3)}$ matrix. The entries of this matrix are only non-zero for mutually exclusive indices, i.e. $i \neq j, i \neq k, i \neq l, j \neq k, j \neq l, k \neq l$. This makes the corresponding term a triple-mode coupling term, which acts as a drive to the i -th mode. For $N = 4$ modes (4.22) can be written as

$$\begin{aligned}
& \mu M_{11} \ddot{q}_1 + \kappa M_{11} \dot{q}_1 + \left(DK_{11} + N_x C_{11}^{(x)} + N_y C_{11}^{(y)} \right) q_1 + G_{11}^{(1)} q_1^3 \\
& \quad + \left(G_{112}^{(2)} q_2^2 + G_{113}^{(2)} q_3^2 + G_{114}^{(2)} q_4^2 \right) q_1 = -G_{1234}^{(3)} q_2 q_3 q_4 \\
& \mu M_{22} \ddot{q}_2 + \kappa M_{22} \dot{q}_2 + \left(DK_{22} + N_x C_{22}^{(x)} + N_y C_{22}^{(y)} \right) q_2 + G_{22}^{(1)} q_2^3 \\
& \quad + \left(G_{221}^{(2)} q_1^2 + G_{223}^{(2)} q_3^2 + G_{224}^{(2)} q_4^2 \right) q_2 = -G_{2134}^{(3)} q_1 q_3 q_4 \\
& \mu M_{33} \ddot{q}_3 + \kappa M_{33} \dot{q}_3 + \left(DK_{33} + N_x C_{33}^{(x)} + N_y C_{33}^{(y)} \right) q_3 + G_{33}^{(1)} q_3^3 \\
& \quad + \left(G_{331}^{(2)} q_1^2 + G_{332}^{(2)} q_2^2 + G_{334}^{(2)} q_4^2 \right) q_3 = -G_{3124}^{(3)} q_1 q_2 q_4 \\
& \mu M_{44} \ddot{q}_4 + \kappa M_{44} \dot{q}_4 + \left(DK_{44} + N_x C_{44}^{(x)} + N_y C_{44}^{(y)} \right) q_4 + G_{44}^{(1)} q_4^3 \\
& \quad + \left(G_{441}^{(2)} q_1^2 + G_{443}^{(2)} q_3^2 + G_{443}^{(2)} q_3^2 \right) q_4 = -G_{4123}^{(3)} q_1 q_2 q_3
\end{aligned} \tag{4.23}$$

In the next chapter we will further study the dynamics of a plate with dimensions typical for a MEMS system. The simulations will be based on the four mode system in (4.23). We choose to limit the study to four modes because experimental data in [5] does not indicate the presence of any higher order modes. Further the numerical study by Ilanko [7] shows only negligible differences between a four-mode and a nine-mode model.

4.3 Critical Stress

An important parameter for bistable MEMS is the critical stress N_{cr} for which the membrane starts to buckle. We follow an energy approach to calculate the critical static load of the first buckling mode for a square plate with $L = L_x = L_y$ [13]. The axial stress components N_x and N_y are assumed to be equal $N = N_x = N_y$.

The external potential energy V_e of the plate is defined as

$$V_e = \int_0^L \int_0^L \frac{N}{2} \left[\left(\frac{\partial w}{\partial x} \right)^2 + \left(\frac{\partial w}{\partial y} \right)^2 \right] dx dy \quad (4.24)$$

and we assume that the shape of the first buckling mode corresponds to ϕ_1 given by eq. (4.8),

$$w = A \cos(\omega t) \left(1 - \cos \frac{2\pi x}{L} \right) \left(1 - \cos \frac{2\pi y}{L} \right). \quad (4.25)$$

where the mode oscillates at frequency ω with a constant amplitude A . By solving the double integral in (4.24) we can express the potential energy of the first buckling mode due to the external axial load as

$$V_e = 3\pi^2 N A^2 \cos^2(\omega t). \quad (4.26)$$

Similarly, we find the kinetic energy of the first mode ϕ_1 ,

$$T = \int_0^L \int_0^L \frac{\mu}{2} \left(\frac{\partial w}{\partial t} \right)^2 dx dy, \quad (4.27)$$

which is evaluated as

$$T = \frac{9L^2 m A^2 \omega^2 \sin^2(\omega t)}{8}. \quad (4.28)$$

The bending energy U_b of the plate for the first mode ϕ_1 ,

$$U_b = \int_0^L \int_0^L \frac{D}{2} \left[\left(\frac{\partial^2 w}{\partial x^2} \right)^2 + \left(\frac{\partial^2 w}{\partial y^2} \right)^2 + 2\nu \frac{\partial^2 w}{\partial x^2} \frac{\partial^2 w}{\partial y^2} + 2(1 - \nu) \left(\frac{\partial^2 w}{\partial x \partial y} \right)^2 \right] dx dy, \quad (4.29)$$

becomes

$$U_b = \frac{16\pi^4 DA^2 \cos^2(\omega t)}{L^2}. \quad (4.30)$$

Equating kinetic energy to the sum of potential energy due to bending and loading yields the oscillation frequency

$$\omega^2 = \frac{8\pi^2(16\pi^2 D + 3NL^2)}{9L^4 m \tan^2(\omega t)}. \quad (4.31)$$

The onset of buckling can be described by the resonant frequency of the first mode reaching zero. By setting ω to zero, the critical stress N_{cr} of the first buckling mode is determined as

$$N_{\text{cr}} = -\frac{16\pi^2 D}{3L^2}. \quad (4.32)$$

4.4 Elastic Potential Energy

The potential energy that is connected to the elasticity of the plate is a useful tool to understand the concept of bistability. We can easily derive it from the equations of motion in (4.23). To understand the basic behavior of bistable plates the potential energy of the first eigenmode is sufficient. Therefore we only view the first equation of (4.23) and set all inter-mode coupling terms to zero $q_2 = q_3 = q_4 = 0$. This leaves us with

$$\mu M_{11} \ddot{q}_1 + \kappa M_{11} \dot{q}_1 + \left(DK_{11} + N_x C_{11}^{(x)} + N_y C_{11}^{(y)} \right) q_1 + G_{11}^{(1)} q_1^3 = 0 \quad (4.33)$$

Comparing (4.33) to the equation of motion of a simple mass-spring system

$$m\ddot{x} + \kappa\dot{x} + kx = F \quad (4.34)$$

we can determine the stiffness of our system to be

$$k = DK_{11} + N_x C_{11}^{(x)} + N_y C_{11}^{(y)} + G_{11}^{(1)} q_1^2. \quad (4.35)$$

The potential energy due to the elasticity can now be easily derived as

$$\begin{aligned} V &= \int k q_1 dq_1 \\ V &= \int (DK_{11} + N_x C_{11}^{(x)} + N_y C_{11}^{(y)} + G_{11}^{(1)} q_1^2) q_1 dq_1 \\ V &= (DK_{11} + N_x C_{11}^{(x)} + N_y C_{11}^{(y)}) \frac{q_1^2}{2} + G_{11}^{(1)} \frac{q_1^4}{4} \end{aligned} \quad (4.36)$$

We will use this expression to plot the double-well potential of a buckled square plate in section 6.1.

Chapter 5

Comparison of Numerical Integration Algorithms

To solve the differential equations that describe the dynamic behavior of thin plates we use numerical integration. The simulation framework is entirely written in python using numerical integration algorithms provided by the *scipy* function *solve_ivp* from the *scipy.integrate* sub-package. This function contains implementations of various state of the art solvers for initial value problems of differential equations systems. There are explicit solvers from the Runge-Kutta family ("RK23", "RK45", "DOP853") for non-stiff, and implicit solvers ("Radau", "BDF") for stiff problems. The "LSODA" solver has automatic stiffness detection. Since we don't know if our problem is stiff, we conduct a series of experiments to choose a solver that is suited for our problem. In order to build intuition for the behavior of the different algorithms, we compare the results achieved when simulating the same time series with each one. Figure 5.1 shows example simulation results for all considered algorithms. The relative error tolerance (rtol) controls the error relative to the deflection w . For fig. 5.1 we use a setting of $\text{rtol}=10^{-6}$. In the plots we see the deflection w of the first mode of vibration ϕ_1 simulated over a time period of $400 \mu\text{s}$. The example simulation result used is the same one that can be seen in fig. 6.5(a) in chapter 6. Detailed information on the simulation result can be found there. What is relevant for this analysis is that we see the plates deflection crossing zero a number of times, which means the membrane switches from one to the other ground state. We notice that until about $250 \mu\text{s}$ (dashed vertical line in the plots) all simulation results are nearly identical. After this time period there are clearly

visible deviations between the different algorithms with switching events appearing at different points in time.

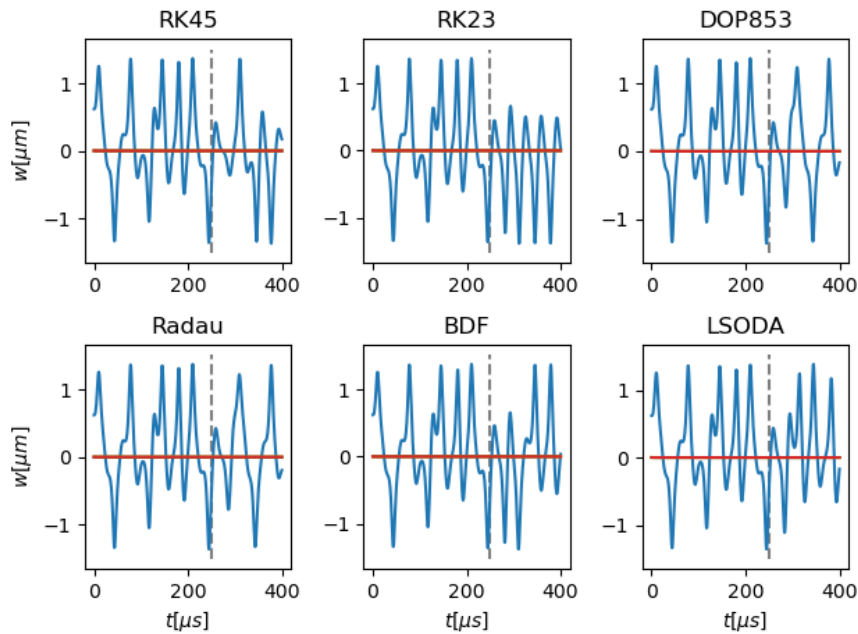


Figure 5.1: Comparison of simulation results with $\text{rtol}=10^{-6}$ for the numerical solvers "RK45", "RK23", "DOP853", "Radau", "BDF" and "LSODA". The simulation parameters are the same as for fig. 6.5(a).

In figure 5.2 we can see the same example simulation for a lower relative error tolerance of $\text{rtol}=10^{-9}$. Now all the simulation results match and we do not observe any visible deviations from each other. What we do notice, is that the "Radau" and "DOP853" algorithms already showed this more precise results for the higher error tolerance setting. We will therefore use the "Radau" algorithm as a reference for further experiments.

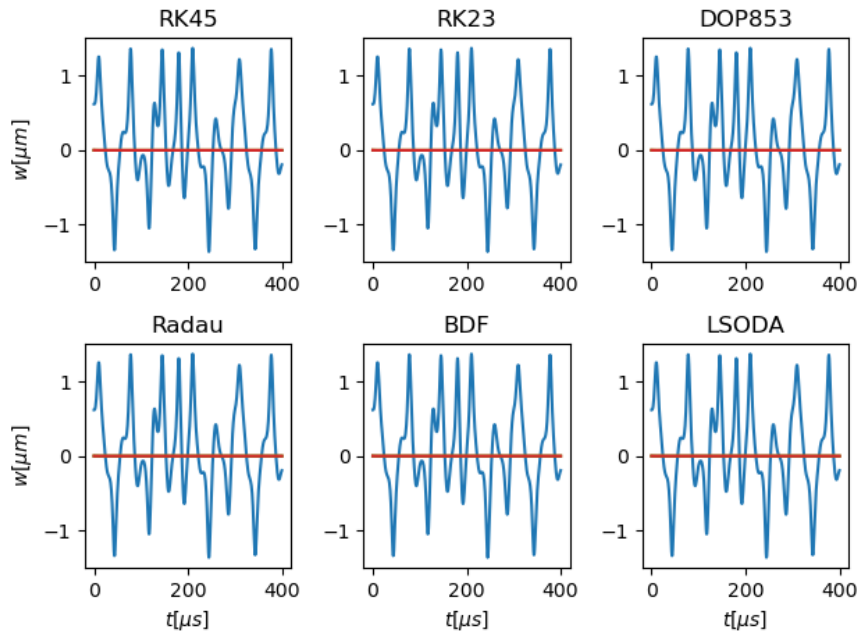


Figure 5.2: Comparison of simulation results with $\text{rtol}=10^{-9}$ for the numerical solvers "RK45", "RK23", "DOP853", "Radau", "BDF" and "LSODA". The simulation parameters are the same as for fig. 6.5(a).

Next we want to check the convergence of the algorithms. The experiment we use is to repeat the same simulation for each algorithm, while decreasing the relative error tolerance by one magnitude each step. We then measure the deviation of the calculated membrane midpoint deflection to the last step. If the algorithm is convergent the deviation from the last simulation should decrease with each repeat. Figure 5.3 shows the absolute difference to the previous rtol setting for relative error tolerances from 10^{-4} to 10^{-12} for each algorithm. This experiment shows convergent behavior for all tested algorithms.

Since low error tolerances correspond with high integration times we need to test the performance of the algorithms with higher error tolerances. For this test we choose simulation parameters that do not result in any switching event over the whole simulation period and solve the initial value problem with the Radau algorithm, using a low relative error tolerance of $\text{rtol} = 10^{-12}$. Next we solve the same problem with all algorithms with $\text{rtol} = 10^{-8}$ and compare the error that the algorithms accumulate over time, by adding up the difference in midpoint deflection at each integration step. The reason for choosing a point with no switching event is, that

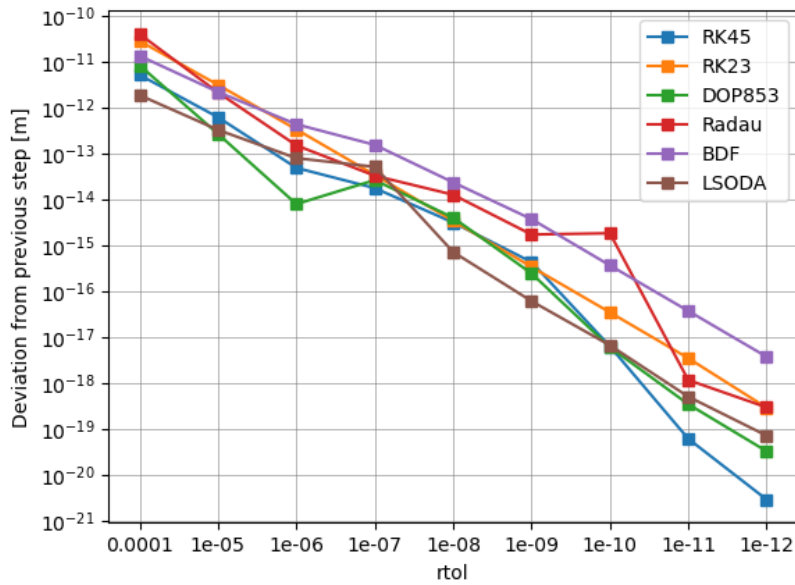


Figure 5.3: Convergence of numerical integration algorithms

small deviations can lead to switching events being delayed, which leads to high errors since switching changes the membrane deflection drastically. This however would limit our perception of the error growth rate over time. Figure 5.4 shows the cumulative error over time of all tested algorithms. We see that the Radau, RK45 and DOP853 algorithms outperform the rest, however all cumulative error values over 400 μs of integration time and 700 integration steps are less than 10^{-11}m . This means at each step the error in the midpoint deflection is in the order of 10^{-14}m , which is negligible compared to membrane deflections of about $10\ \mu\text{m}$. Figure 5.5 shows the cumulative error compared to Radau $\text{rtol}=10^{-12}$ after 400 μs for each algorithm with decreasing relative error tolerance. We see that with decreasing error tolerance the cumulative error decreases for all algorithms. Therefore we can assume that the algorithms all converge towards the same result.

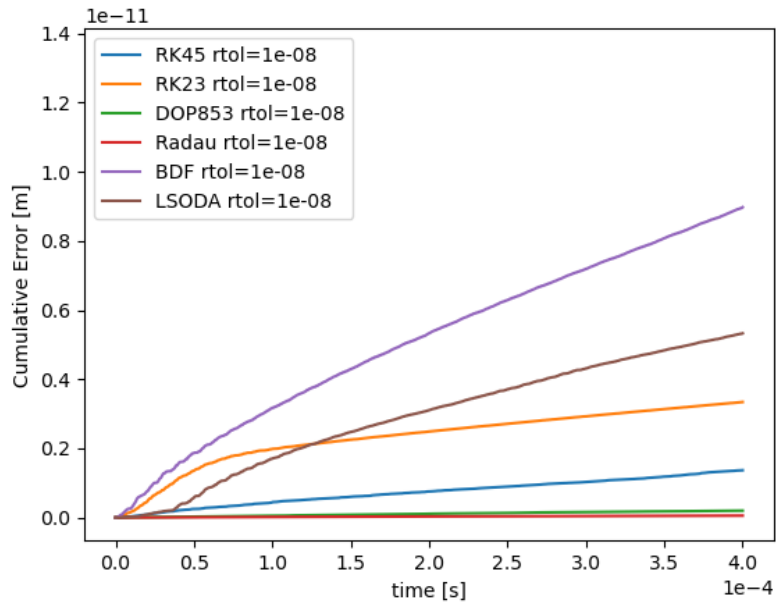


Figure 5.4: Cumulative error over time compared to Radau with $\text{rtol}=10^{-12}$

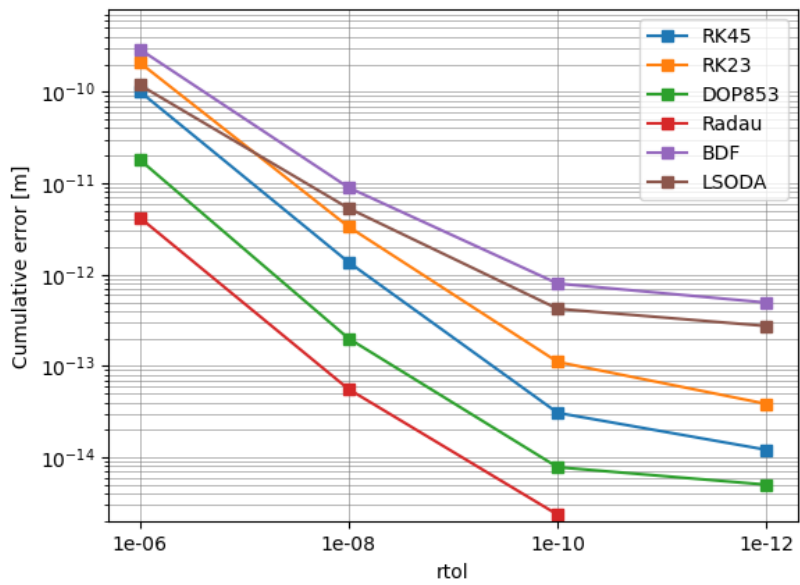


Figure 5.5: Cumulative error after $400\ \mu\text{s}$ of integration time for decreasing rtol values compared to Radau with $\text{rtol}=10^{-12}$

Another important measure is the execution time of the algorithms. This measurement is of course dependant on the machine the code is executed on. However since our goal is to qualitatively compare the execution times of all algorithms to each other this is not an issue. Figure 5.6 shows the execution time rise of all the algorithms for lowering relative error tolerances. We can see that the Radau and

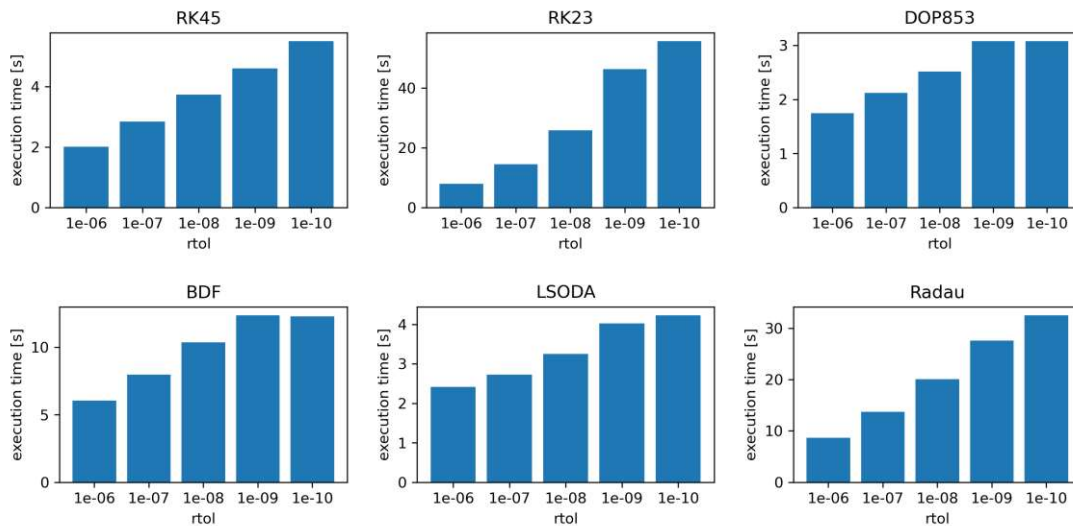


Figure 5.6: Algorithm execution times for decreasing values of rtol

RK23 and BDF algorithms have comparatively high execution times making them undesirable for calculating stability maps with thousands of points. The rest of the algorithms perform very similarly, with the DOP853 algorithm consistently being the fastest. In summary it can be said that all algorithms are convergent and produce similar results. Since the goal of this work is establishing the mathematical model and visualizing the system dynamics over broad parameter spaces, execution time will be prioritized over precision. All results in this work have been calculated using the RK45 algorithm with a relative error tolerance setting of $rtol = 10^{-8}$.

Chapter 6

Simulation Results

To gather knowledge about the general dynamics at place in bistable MEMS we will conduct experiments on the system of differential equations described in (4.23). We define the system parameters to resemble the systems that have been experimentally studied in [5] and [4]. The system investigated will be a square plate with a side

Table 6.1: Simulation parameters

Parameter	Value
Side length L	700 μm
Thickness h	3.50 μm
Damping rate κ	700 $\text{kg m}^{-2} \text{s}^{-1}$
Young's modulus E	165 GPa
Poisson's ration ν	0.22
Density ρ	2330.0 kg m^{-3}
Pre-stress $ \sigma^{(0)} $	≤ 60 MPa
Piezo-stress $ \sigma^{(p)} $	≤ 80 MPa

length of $L = L_x = L_y$ of 700 μm and a thickness h of 3.5 μm . We assume the plate to consist of an isotropic material with the same elastic properties as silicon. The material parameters of silicon are taken from ref. [2]. We model the pre-stress and the piezo-stress to be equal for both axes $N = N_x = N_y$. It should be noted that for the ease of reading the stress-resultants N will often be referred to as the stresses. For the damping rate κ we choose a value of 700 $\text{kg m}^{-2} \text{s}^{-1}$ which corresponds to the typical damping of a MEMS resonator in a gaseous environment like air. In

experiments pre-stresses of up to $\sigma^{(0)} = -64.9$ MPa [4] and piezo-stresses of up to $\sigma^{(p)} = \pm 80$ MPa [3] have been documented. Plate pre-stresses in this analysis will be between 19 MPa and 59 MPa and we will limit the piezo-stress to $\sigma^{(p)} = \pm \sigma^{(0)}$. This limitation is chosen in order to avoid a change from compressive to tensile stress in the plate due to the piezo-stress. All parameters used in simulations are summarized in table 6.1. The plate dynamics will be investigated by numerically solving the DEQ system (4.23). Table ?? in the appendix shows the computed ODE coefficients used for this analysis. We use an explicit Runge-Kutta method of order 5(4) as a solver. An evaluation of different different solvers and solver parameters leading to the chosen solver can be found in chapter 5.

6.1 Static Analysis

In section 4.3 the critical stress N_{cr} for a plate axially loaded on both sides is calculated, resulting in expression (4.32). For the parameters in table 6.1 the critical stress is evaluated as $N_{cr} = 66.55 \text{ N m}^{-1}$ which is equal to $\sigma_{cr} = 19.01$ MPa. We simulate the plate dynamics in order to find the stable buckling mode for different amounts of pre-stress, and compare the results with this calculated value. Figure 6.1 shows the maximum deflection of each mode as a function of the pre-stress $N^{(0)}$. We get this deflection by multiplying the generalized coordinates by the maximum of the associated mode shapes.

$$w_i(t) = q_i(t) \max_{x,y \in [0,L]} \phi_i(x,y) \quad (6.1)$$

As an initial condition for this simulation we assume all modes to have an initial deflection of 1 nm. This non-zero initial deflection accounts for the influence of noise on the system. If we analyze the system of differential equations (4.23) we notice that with initial conditions $q_i = \dot{q}_i = 0$ for all i , the systems deflection will always stay zero. However in practice these initial conditions will never be met, since the system will always be under the influence of different sources of noise and environmental conditions that cause deviations in the deflection. Studies by Murphy [9] and Ilanko [7] both find that small initial deflections have a significant impact on the critical buckling load of thin plates. The piezo-stress and all time derivatives are set to zero for this experiment. The x-axis of figure 6.1 is scaled by

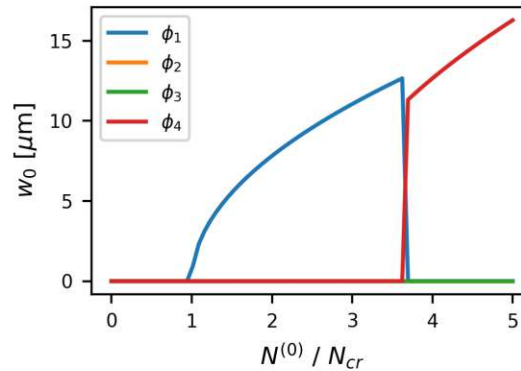


Figure 6.1: Static deflection amplitudes of the first four modes for static pre-stress values of $0 \leq N^{(0)} \leq 5N_{cr}$.

the calculated value for N_{cr} . We see a good agreement between the simulation and the calculated critical stress, with the plate showing a significant deflection of the first mode ϕ_1 for $N^{(0)} \geq N_{cr}$. For increasing pre-stress we see the static deflection growing. We also see that the stable buckling mode changes from ϕ_1 to ϕ_4 from a pre-stress of $N^{(0)} \approx 3.7N_{cr}$ on. The ϕ_2 and ϕ_3 modes do not show any deflection in this experiment. This is due to the symmetrical loading of the plate. For uniaxial loading with either $N_x = 0$ or $N_y = 0$ these modes take over the role of the second buckling mode.

An intuitive way to gain understanding of the behavior of bistable MEMS is to describe the buckled membrane in terms of its elastic potential energy. For this analysis we will only study plates with $N \leq 3N_{cr}$. This means ϕ_1 will be the static buckling mode. Since the static deflections of all other modes are negligible for the chosen pre-stress we can use the simplified expression for the elastic potential energy described in section 4.4. With the coefficients from table A.1 we re-write (4.36) as

$$V = \frac{16\pi^4 D}{L^2} \left(1 - \frac{N}{N_{cr}}\right) q_1^2 + \frac{9\pi^4 E h}{4L^2} q_1^4 \quad (6.2)$$

Figure 6.2 shows this elastic potential V as a function of the midpoint displacement of the first mode w_1 for increasing amounts of pre-stress $N^{(0)}$. If the pre-stress is below or equal to N_{cr} the elastic potential is parabolic and has a single minimum at $w_1 = 0$. For pre-stress values $N > N_{cr}$ the potential becomes the double-well

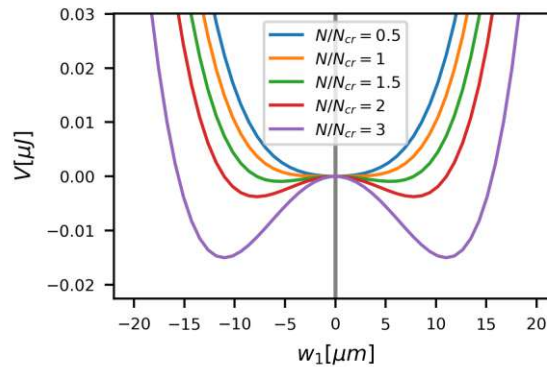


Figure 6.2: Elastic potential energy for $0 \leq N^{(0)} \leq 3N_{cr}$.

potential that is characteristic for bistable MEMS. Two local minima develop, that correspond to the two stable ground-states. The minima in the potential energy plot develop at the two stable deflections. These values correspond to the static deflection amplitudes in figure 6.1. If we assume a pre-stress $N^{(0)} = 3N_{cr}$ figure 6.1 shows a deflection of about $11 \mu\text{m}$, which is the same deflection at which the two minima are displayed for the corresponding plot in fig. 6.2. In order to induce snap-through the potential barrier between these two minima needs to be overcome. While describing the membranes behavior using the first modes elastic potential energy is a good way to gain intuitive understanding, a multi-modal model is still needed to accurately model the system dynamics. For this reason all simulations are based on the multi-modal model defined in (4.23).

6.2 Initiation of Snap-through

In order to use bistable MEMS plates as actuators it needs to be possible to externally control their deflection. As described in section 3.1 this is done by a piezoelectric transducer which influences the mechanical stress when applying a voltage. The change in mechanical stress is directly proportional to the applied voltage. We model this effect with the variable piezo-stress $N^{(p)}(t)$. Varying this stress over time enables us to induce parametrically excited oscillations of the membrane deflection. These oscillations can cause snap-through if the oscillation amplitude is high enough to overcome the potential barrier between the two stable configurations. In theory it is also possible to induce snap-through without exciting any oscillations. In a quasi-static regime there are two other ways of actuating the

membrane. Since the possible stress change that can be induced by the piezo-layer is larger than the static pre-stress, it is possible to fully compensate the pre-stress. This would cause the membrane to flatten out and lose its bistability temporarily. Re-introducing the mechanical stress by removing the piezo-stress will make the plate buckle once again. For a perfectly symmetrical double-well potential this would mean the plate would randomly fall into one of its stable configurations. In the piezoelectric bistable MEMS described in [3] however the piezo-stack introduces an asymmetry to the potential, causing one of the two states to be preferred. This means simply compensating the pre-stress and subsequently reintroducing it is not a reliable means of switching the membrane state, since it will only work one way. The second quasi-static way of introducing snap-through is increasing the piezo-stress until the mechanical stress exceeds the critical stress for the second buckling mode. Reducing the piezo-stress after the second buckling mode has stabilized will cause the first buckling mode to become the stable configuration again. The transition between the static buckling modes causes considerable oscillations and the first buckling mode can stabilize in either of its two stable configurations.

Both quasi-static ways of switching are not suited for actuation applications, since the state the membrane is in after the switching process is unpredictable. The asymmetry in the elastic potential that piezoelectric bistable MEMS membranes typically show ultimately makes these schemes of actuation nonviable.

6.2.1 Continuous Harmonic Excitation

We model the piezoelectric excitation of the plate with the piezo-stress $N^{(p)}(t)$. Modulating this stress over time enables us to induce oscillations in the plate deflection, which can cause snap-through. We will first analyze the plates behavior under continuous harmonic excitation, defining the time dependant piezo-stress as

$$N^{(p)}(t) = N_0^{(p)} \sin(2\pi ft)\Theta(t) \quad (6.3)$$

$N_0^{(p)}$ is the excitation amplitude and f is the excitation frequency. The Heaviside step function Θ ensures that the excitation signal is zero for $t \leq 0$. We choose a sine excitation signal to avoid discontinuous jumps of the excitation signal at $t = 0$. An important property for actuation is how fast an excitation signal can induce snap-through. We therefore simulate the plate dynamics for different sets

of excitation amplitude and excitation frequency over a time frame of $400 \mu\text{s}$. We define the initial snap-through time T_s as the time until the deflection of the first mode reaches zero for the first time $w_1(T_s) = 0$. This definition is sufficient in the pre-stress regime $N^{(0)} < 3.7N_{cr}$ where only the first mode ϕ_1 shows a static deflection. Figure 6.3 illustrates the dependency of T_s on the excitation amplitude $N^{(p)}$ and excitation frequency f for a static pre-stress of $N^{(0)} = 1.1N_{cr}$. The white

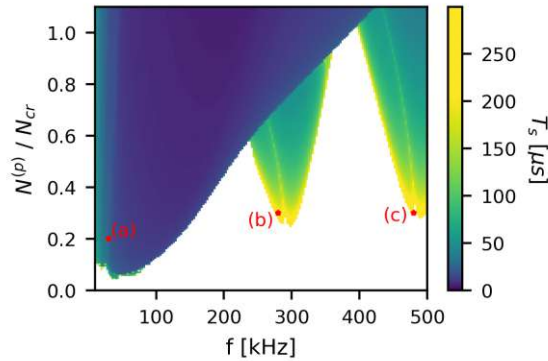


Figure 6.3: Initial snap-through time for $N^{(0)} = 1.1N_{cr}$

regions in the map correspond to parameter combinations where no snap-through is observed during the whole time frame. In the colored regions one or more snap-through events are observed. The map is being separated into three distinct tongues. The first tongue reaches down to drive amplitudes of $N^{(p)} = 0.04 N_{cr}$ at a drive frequency of $f = 35.5 \text{ kHz}$. In this tongue the snap-through time is very homogeneous and well below $50 \mu\text{s}$. Only a zoom-in shown in fig. 6.4 reveals a finer structure at the border of this tongue. The middle tongue in fig. 6.3 reaches

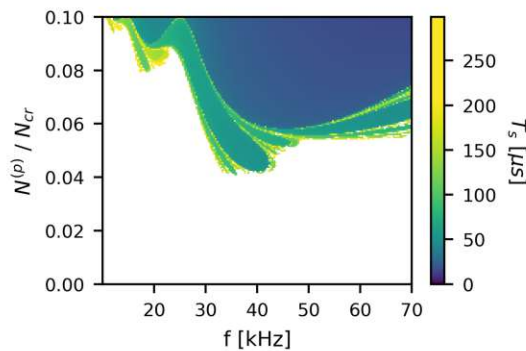


Figure 6.4: Zoom into the border region of the first tongue in fig. 6.3.

down to $N^{(p)} = 0.25 N_{cr}$ at an excitation frequency of $f = 297$ kHz, while the right tongue only reaches down to and to $N^{(p)} = 0.28 N_{cr}$ at $f = 489$ kHz. In these tongues the initial snap-through times are much larger, even reaching values above $250 \mu\text{s}$. Figure 6.5 shows three example modal deflection time series. Each of them shows dynamics typical for one of the three tongues. The corresponding points for each time series are also highlighted in figure 6.3. In figure 6.5(a) we

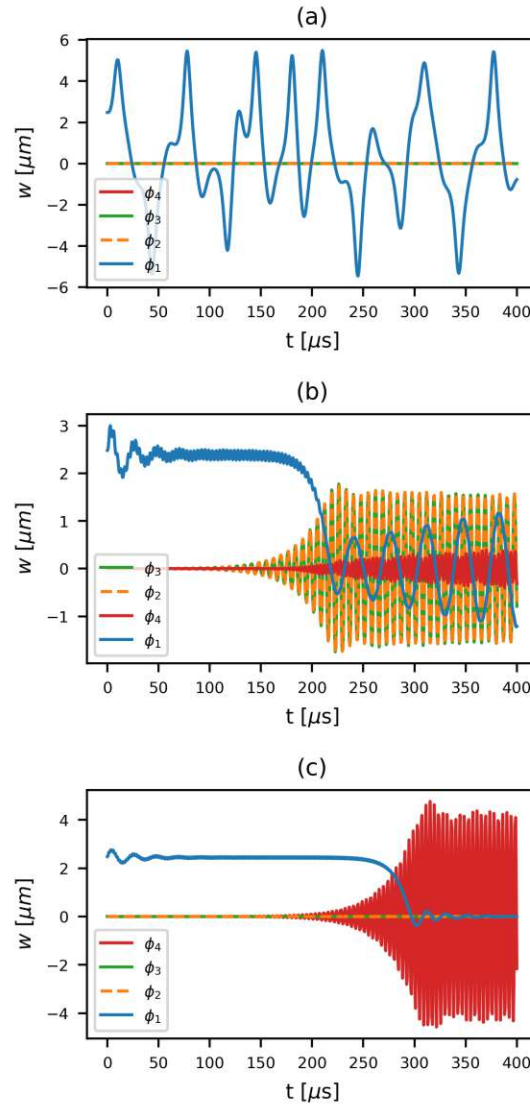


Figure 6.5: Example time series of the modal maximum deflections $w_i(t)$: (a) $f_p = 30$ kHz, $N_0^{(p)} = 0.2N_{cr}$, (b) $f = 280$ kHz, $N_0^{(p)} = 0.3N_{cr}$, (c) $f = 480$ kHz, $N_0^{(p)} = 0.3N_{cr}$.

observe a purely uni-modal behavior with ϕ_1 being the only mode that shows significant deflection. The initial snap-through event happens at $T_s = 26 \mu\text{s}$ and the deflection immediately snaps back to positive deflections. We then observe further oscillations of ϕ_1 with snap-through events at irregular points in time. The middle tongue shows dynamics that are exemplified by figure 6.5(b). Here we at first only observe small oscillations of ϕ_1 around the equilibrium. Starting from about $150 \mu\text{s}$ we can see growing oscillations of ϕ_2 and ϕ_3 while ϕ_1 starts moving away from its equilibrium. ϕ_1 reaches zero deflection at $T_s = 215 \mu\text{s}$, after which it does not return to its equilibrium, but rather oscillates around $w_1 = 0$ at a rather low frequency of about 26.5 kHz . ϕ_2 and ϕ_3 oscillate at 140 kHz , which is half of the excitation frequency. This matches the behavior of parametric resonance described in section 3.2. The oscillation amplitude of ϕ_2 and ϕ_3 starts leveling out right after the initial snap-through time T_s . Additionally ϕ_4 shows growing oscillations, which become significant as ϕ_1 moves away from its initial deflection. The dynamics shown in figure 6.5(c) are similar. Here ϕ_4 takes the place of modes ϕ_2 and ϕ_3 and shows significant oscillations after about $200 \mu\text{s}$. Mode ϕ_1 moves away from its initial deflection after $250 \mu\text{s}$. However it does not show any significant oscillations after it reaches $w_1 = 0$. Modes ϕ_2 and ϕ_3 do not show any significant deflection at all. For the use in MEMS actuators uni-modal dynamics are preferred, since multi-modal dynamics can among other things affect how surrounding fluids are actuated. This can for example cause unwanted signal distortions in ultrasound generation. To gain understanding of the multi-modal dynamics our system shows we introduce the modal participation factor λ_i . We define λ_i as the time averaged absolute deflection of a mode denoted by $\langle |\cdot| \rangle$ in relation to the static deflection of mode ϕ_1 at $t = 0$.

$$\lambda_i = \frac{\langle |q_i(t)| \rangle}{q_1(0)} \quad (6.4)$$

The modal participation factors for the data in figure 6.3 are shown in figure 6.6. The black border in the images represents the border between regions with, and without snap-through in figure 6.3. It is immediately visible that the dynamics in the left tongue are almost uni-modal. There is only a minor participation of modes ϕ_2 and ϕ_3 in this region. The dynamics of the middle tongue are dominated by ϕ_2 and ϕ_3 . It is notable that the multi-modal dynamics of the middle tongue reach far

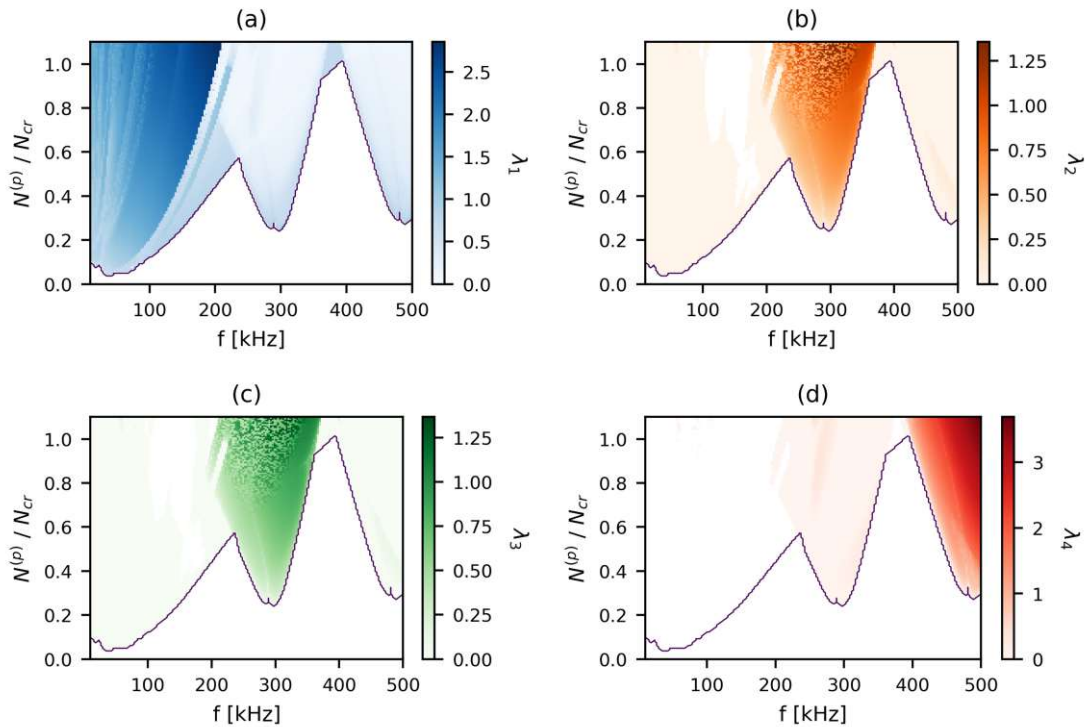


Figure 6.6: Modal participation factors λ_1 (a), λ_2 (b), λ_3 (c) and λ_4 (d) for the data in fig. 6.3

into the region that appeared homogeneous in figure 6.3. In the right tongue the high values of λ_4 indicate that the dynamics are mainly dependant on the ϕ_4 mode.

The static analysis showed that a higher pre-stress $N^{(0)}$ leads to a higher static deflection. As more deflection is highly desirable in actuators we need to study the influence of pre-stress on the snap-through dynamics. Figure 6.7 shows initial snap-through time maps for four different amounts of pre-stress up to $N^{(0)} = 3.0N_{cr}$. We see, that the initial snap-through times remain similar for each pre-stress. However a higher pre-stress generally causes the excitation amplitude that is needed in order to cause snap-through to increase. This makes intuitive sense, since the potential wells of the double-well potential get deeper with increasing pre-stress, causing the potential barrier that needs to be overcome to grow. Another observation we can make, is that the structure of the leftmost tongue gets more complex with increasing pre-stress. The fine structure that was only visible in the zoom-in (fig. 6.4) for $N^{(0)} = 1.1N_{cr}$ takes over more and more of the plots area. A further zoom into figure 6.7(c) reveals an even finer structure. The images in figure 6.8 show a

zoom into the areas highlighted by the red rectangles. A complex structure with a fractal character is revealed. The regions edge is divided into lobes that become smaller the closer they get to the edge of the area where switching is possible. These lobes are separated by cuts where the initial snap-through time is considerably larger or snap-through is not possible at all. Next we will pay attention to the tongue like structure that corresponded with the participation of different modes in figure 6.3. For a pre-stress of $N^{(0)} = 1.5N_{cr}$ these tongues are still clearly separable. With increasing pre-stress the tongues merge into each other until no separable tongues are visible anymore in figure 6.7(d).

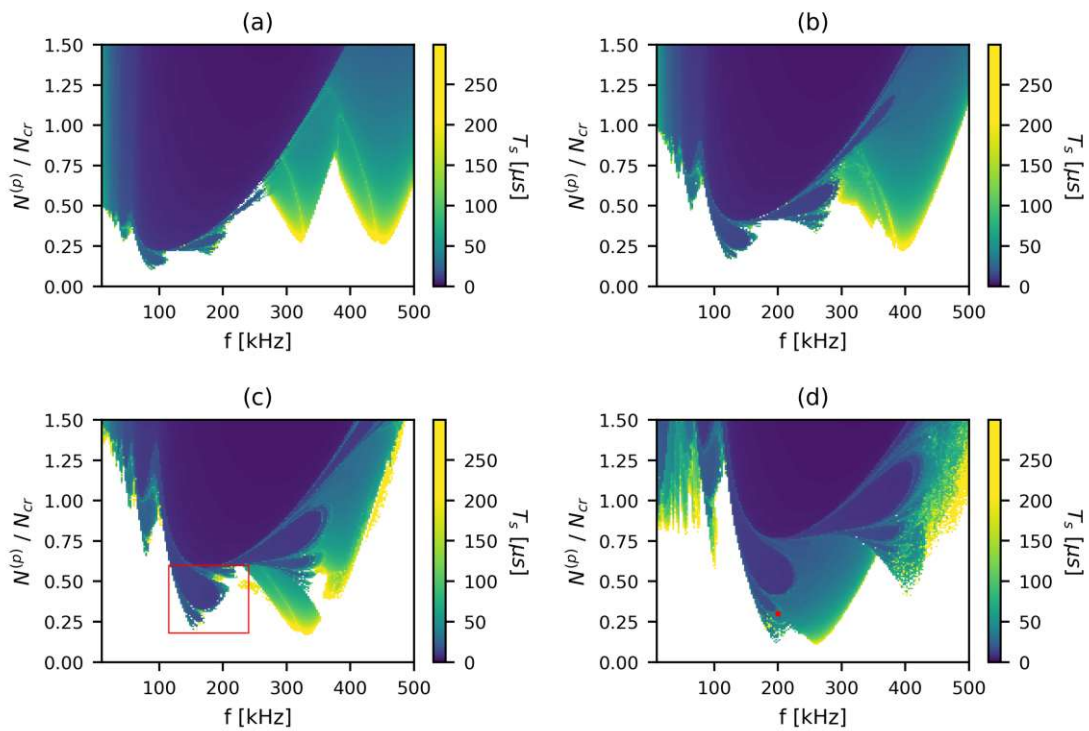


Figure 6.7: Maps of the initial snap-through time for different static pre-stresses ($N^{(0)} = 1.5N_{cr}$ (a), $N^{(0)} = 2.0N_{cr}$ (b), $N^{(0)} = 2.5N_{cr}$ (c), $N^{(0)} = 3.0N_{cr}$ (d)). The red square in (c) marks the zoom-in region in fig. 6.8a.

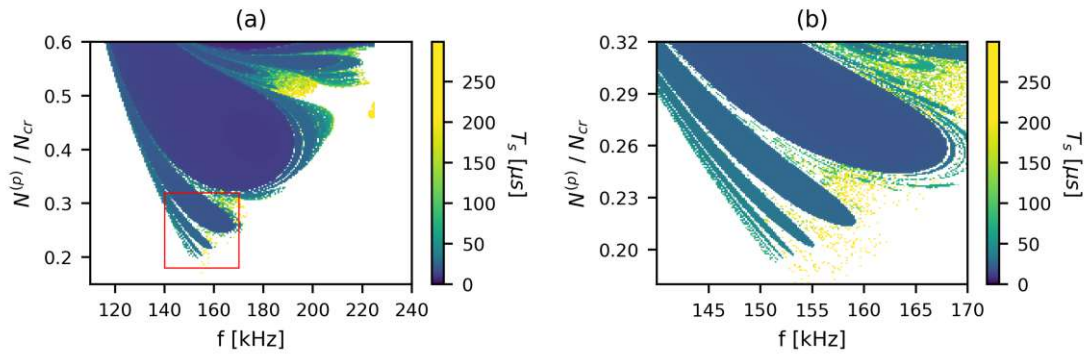


Figure 6.8: Zoom-ins into the initial snap-through time map in fig. 6.7c. The red square in (a) marks that is shown in (b).

For low pre-stress the map was easily separable into areas with uni-modal and multi-modal behavior. For increasing pre-stress this distinction can no longer be made. To illustrate this effect figure 6.9 shows the modal participation factor λ_4 for the data in figure 6.7. Image (a) shows, that for $N^{(0)} = 1.5N_{cr}$ the left tongue is still mostly uni-modal and the influence of the ϕ_4 mode is still concentrated in the rightmost tongue. As the tongue structures merge into one another with increasing pre-stress the dynamics significantly change. The influence of ϕ_4 outside of its original region grows and even lower frequency areas show a significant modal participation factor λ_4 . For a pre-stress of $N^{(0)} = 3N_{cr}$ the multi-mode dynamics with mode ϕ_4 appear homogeneously distributed over the whole map (figure 6.9(d)). Figure 6.10 serves as an example for the complex multi-modal dynamics that take place for a pre-stress of $N^{(0)} = 3.0N_{cr}$. All four considered modes show irregular oscillations and snap-through events happen at non-periodic points in time. The parameters chosen for this example are also highlighted with a red dot in figure 6.7(d).

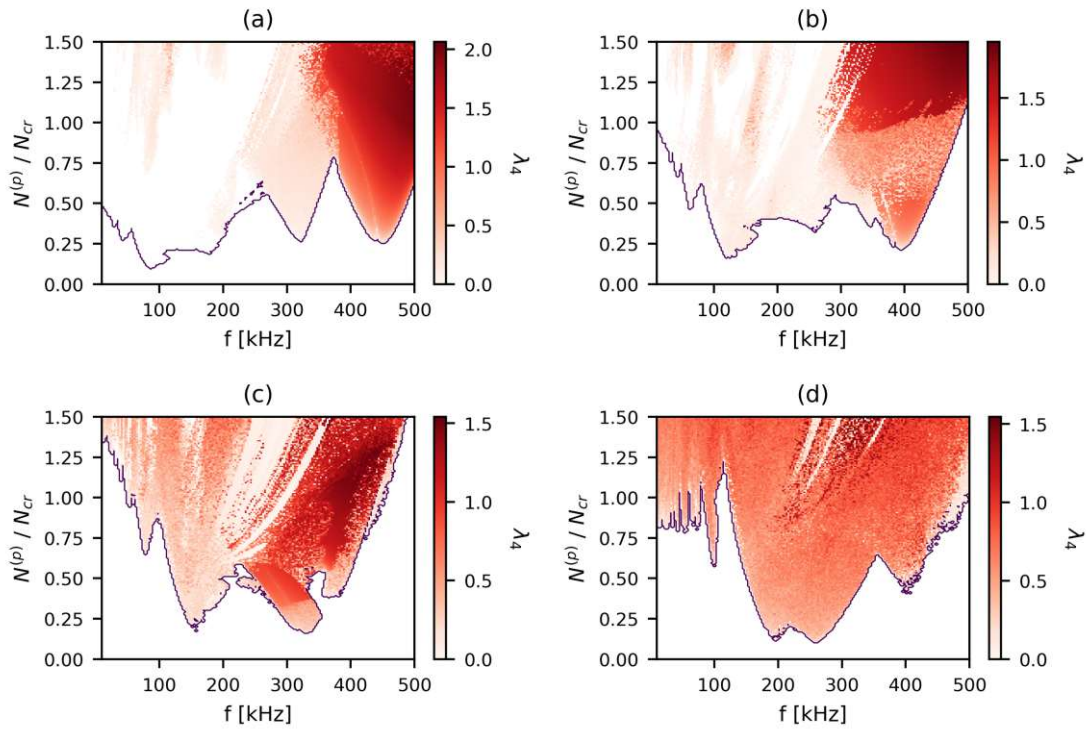


Figure 6.9: Modal participation factor λ_4 for $N^{(0)} = 1.5N_{cr}$ (a), $N^{(0)} = 2.0N_{cr}$ (b), $N^{(0)} = 2.5N_{cr}$ (c) and $N^{(0)} = 3.0N_{cr}$ (d). The borders between the regions with and without snap-through have been emphasized with a solid dark line.

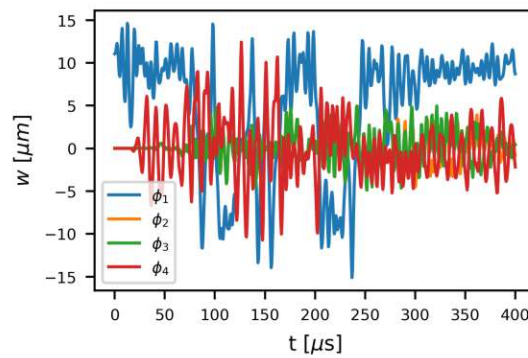


Figure 6.10: Example modal time series for $N^{(0)} = 3.0N_{cr}$, $f_p = 200$ kHz, $N^{(p)} = 0.3N_{cr}$.

6.2.2 Finite Harmonic Pulse Train Excitation

Until now the simulation data was focused on plates excited by a continuous signal. This analysis is useful in order to understand the system dynamics under a continuous load. For actuators however the excitation signal is usually not infinitely long. While continuous excitation signals have their application, for example in ultrasound generation, they do not give us control over the number of snap-through events generated. We can gain control by using a finite pulse train as the excitation signal. An important question for actuation, is the state the system is in after the end of the pulse train when all transients have died out. We define the finite pulse train as

$$N^{(p)}(t) = N_0^{(p)} \sin(2\pi ft) \Pi_n(t, f) \quad (6.5)$$

where Π_n is a rectangular window function with an amplitude of $\max(\Pi_n(t, f)) = 1$ and a length of $T_n = n/f$. This excitation represents a pulse train of n successive sine pulses applied to the structure. Figure 6.11 shows initial snap-through time maps for a pre-stress of $N^{(0)} = 2.5N_{cr}$ and one to four excitation pulses. The pre-stress was chosen to resemble the pre-stress achieved in experiments [4]. In image 6.11(a) we can see that for one pulse the initial snap-through time is very homogeneous over the whole map and no complex structure is visible. However the excitation amplitudes needed to induce snap-through are comparatively high. Adding more excitation pulses the plot gradually starts resembling figure 6.7(c). With each added pulse more regions where snap-through is possible get added. The amplitudes needed to induce snap-through also decrease for each added pulse. The red dots (a) and (b) highlight the points that are illustrated in figure 6.14 as examples for finite pulse train snap-through dynamics.

In order to gain information on the behavior after the first snap-through event we count the number of observed switching events n_s that occur in the simulation window of 400 μ s. For controlled actuation we ideally want our excitation signal to cause exactly one switching event. After the transients died out the excitation can then be repeated. Figure 6.12 maps the number of switching events observed over the parameter space of excitation amplitude and frequency. For one excitation pulse a rather simple image is being displayed. There is one big connected region where only one snap-through event is observed, and several large regions with

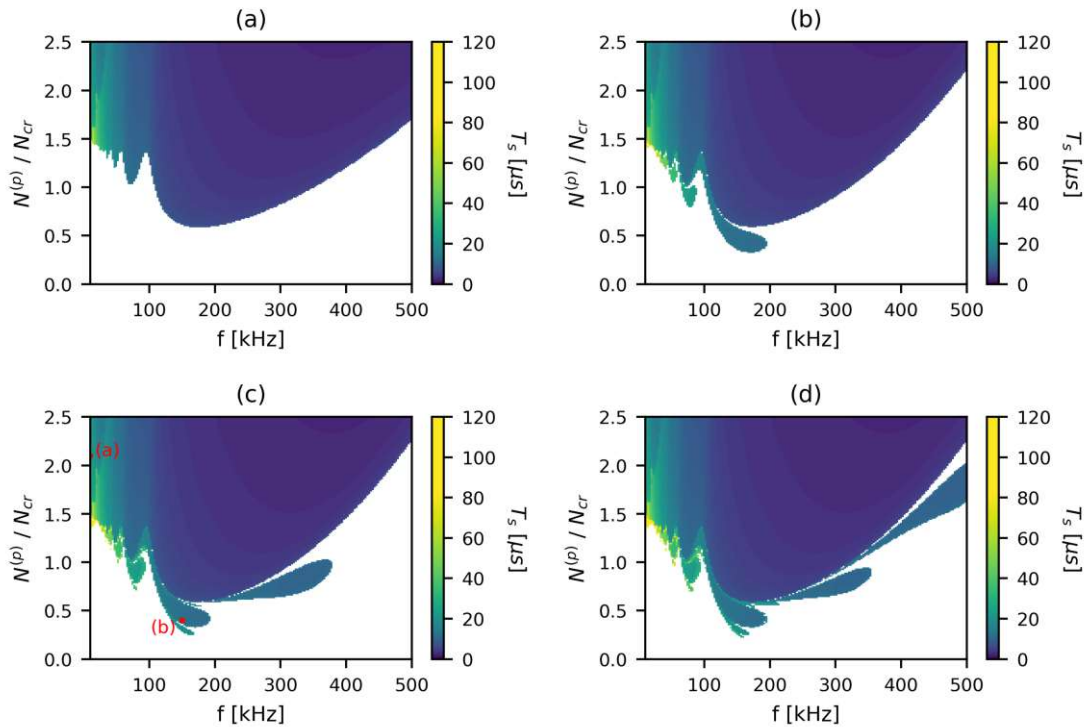


Figure 6.11: Maps of the initial snap-through time for $N^{(0)} = 2.5N_{cr}$ and one (a), two (b), three (c) or four (d) harmonic excitation pulses. The red dots in (c) mark the parameters for which modal time series are displayed in fig. 6.14.

two or more snap-through events. Quite intuitively adding more pulses generally increases the number of snap-through events observed. What can also be observed, is that the structure of the map becomes more complex with more pulses being added. The regions with only one snap-through event become considerably smaller. At the same time the maps are being divided into more and more individual regions with different numbers of switching events, separated by irregularly shaped borders. For controlled actuation this highly segmented map presents a problem. Small deviations in the excitation signal, or environmental conditions can lead to large changes in the switching behavior of the plate. We are therefore left with a trade-off between the excitation amplitudes needed to induce snap-through, and the predictability of the switching dynamics.

What we do not see in any of the maps covering finite pulse train excitation is the regions we associated with the influence of higher order modes. It is therefore worthwhile to again investigate the modal participation factor in order to gain

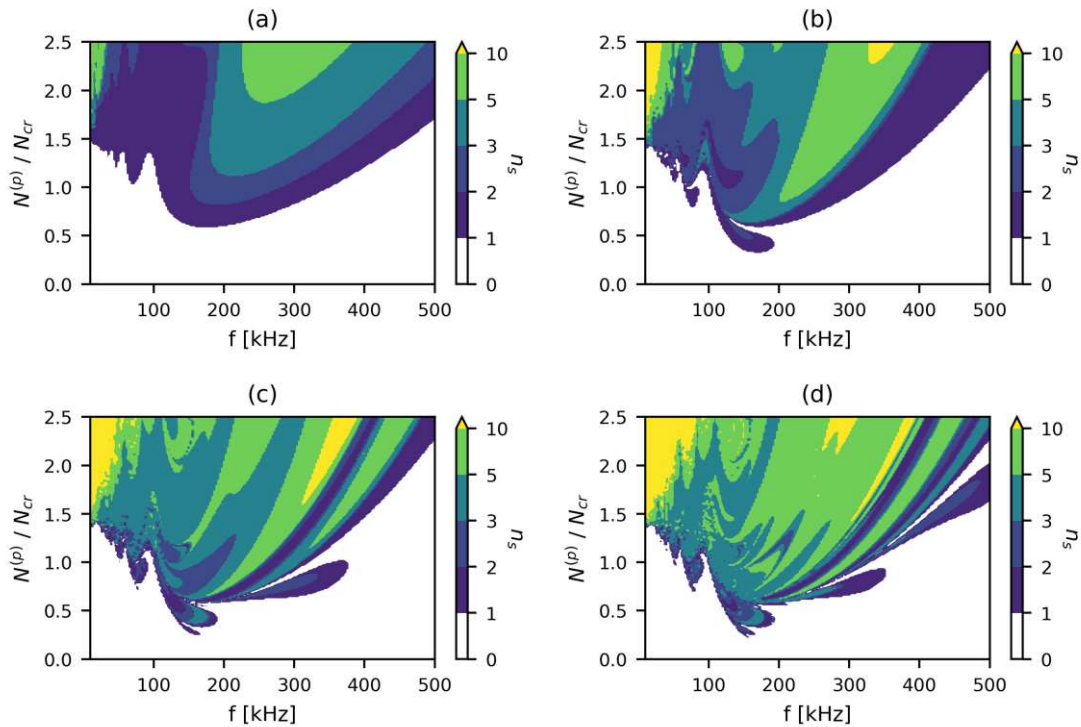


Figure 6.12: Number of switching events after $400\ \mu\text{s}$ for $N^{(0)} = 2.5N_{cr}$ for one (a), two (b) three (c) and four (d) harmonic excitation pulses.

additional understanding. Figure 6.13 displays the participation of the ϕ_4 mode for three excitation pulses. We see a low modal participation factor λ_4 across the majority of the map. Since initial snap-through times caused by higher order modes were in general higher in our analysis of continuous harmonic excitation, we can assume that higher order oscillations need more time to manifest, and are therefore not present when only a small number of excitation pulses is applied. In figure 6.13 we see an area at low frequencies and high excitation amplitudes with a relatively high participation factor λ_4 . This is due to the effects of quasi-static mode jumping. In this area the sum of piezo-stress and pre-stress is high enough to overcome the critical stress for the second order buckling mode. Additionally the excitation frequency is low enough for ϕ_4 to stabilize. Figure 6.14(a) shows an example modal time plot that shows quasi-static mode jumping. The vertical gray lines indicate the length of the excitation cycles. We see the deflection of ϕ_1 slowly rising, until the stress becomes high enough for ϕ_4 to become the stable buckling mode. As the deflection of ϕ_4 rises ϕ_1 becomes unstable and oscillates

with high amplitudes. With the stress reducing ϕ_1 becomes the stable buckling mode again and the deflection of ϕ_4 diminishes. This effect is of course also present when applying a continuous excitation signal. The reason it is not visible in figure 6.9 is twofold. On one hand, the sum of pre-stress and piezo-stress must be large enough in order to reach the critical stress of the second buckling mode ϕ_4 . In fig. 6.9 the maximum piezo-stress is $1.5N_{cr}$ and the sum of pre-stress and piezo-stress only reaches the critical load of the second buckling mode in fig. 6.9(c) and (d). On the other hand, the modal average participation factor is generally higher for continuous excitation, since resonant oscillations of higher order modes have enough time to manifest. This makes it impossible to differentiate between resonant and quasi-static switching in the modal participation maps 6.9.

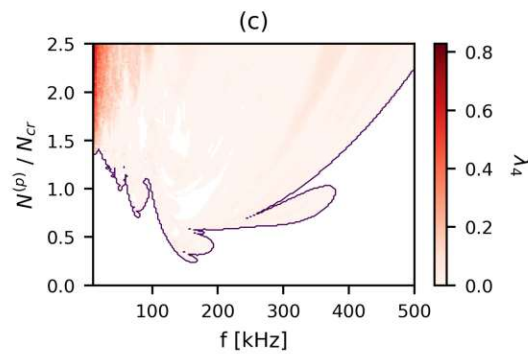


Figure 6.13: Modal participation factor λ_4 for three harmonic excitation pulses at $N^{(0)} = 2.5N_{cr}$

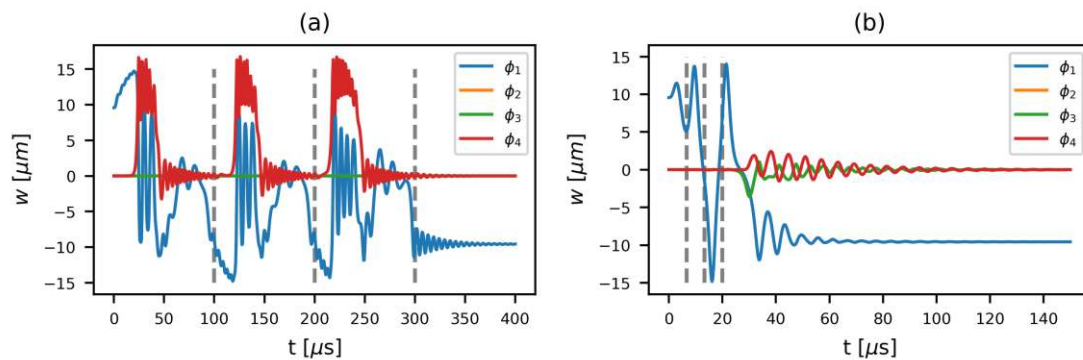


Figure 6.14: Example simulation results for an excitation with three harmonic pulses. (a) $f=10\text{kHz}$ $N^{(p)}/N_{cr} = 2.1$, (b) $f=150\text{kHz}$ $N^{(p)}/N_{cr} = 0.4$,

6.2.3 Finite Rectangular Pulse Train Excitation

In experiments [4] rectangular pulses with an offset applied have been used to induce snap-through in piezoelectrically actuated bistable MEMS. In order to make the results comparable to the ones in section 6.2.2 we will first investigate excitation with a finite rectangular pulse train without any offset. We define this pulse train similarly to (6.5) as

$$N^{(p)}(t) = N_0^{(p)} \text{rect}(2\pi ft) \Pi_n(t, f) \quad (6.6)$$

with

$$\text{rect}(2\pi ft) = \begin{cases} 1 & \text{if } \sin(2\pi ft) \geq 0 \\ -1 & \text{if } \sin(2\pi ft) < 0 \end{cases} \quad (6.7)$$

Figure 6.15 shows the initial snap-through times for an excitation with one to four rectangular pulses. The plate again is under a pre-stress of $N^{(0)} = 2.5N_{cr}$. Comparing the results to figure 6.11 we notice that the excitation amplitudes needed to induce snap-through are reduced, especially for low excitation frequencies. This makes intuitive sense due to the higher harmonic content of a rectangular wave compared to a sine wave. Otherwise we notice similar dynamics. Adding more pulses again adds more regions where snap-through is possible while decreasing the needed excitation amplitudes.

We can again view the number of switching events that occur in a time frame of 400 μs to gain more understanding of the dynamics after the initial snap-through. The behavior is again similar to the one observed when using sine pulses. The most striking difference is again observed for lower excitation frequencies up to about 100 kHz. The number of counted snap-through events in this area drastically increases. Figure 6.17 shows a large influence of mode ϕ_4 in the same area where we notice an increase in switching events. This can be explained with an increased influence of quasi-static mode jumping. Since the rectangular signal instantly reaches its maximum value and stays there longer than the sine wave, the ϕ_4 mode has more time to stabilize. That means quasi-static mode jumping can appear at higher frequencies.

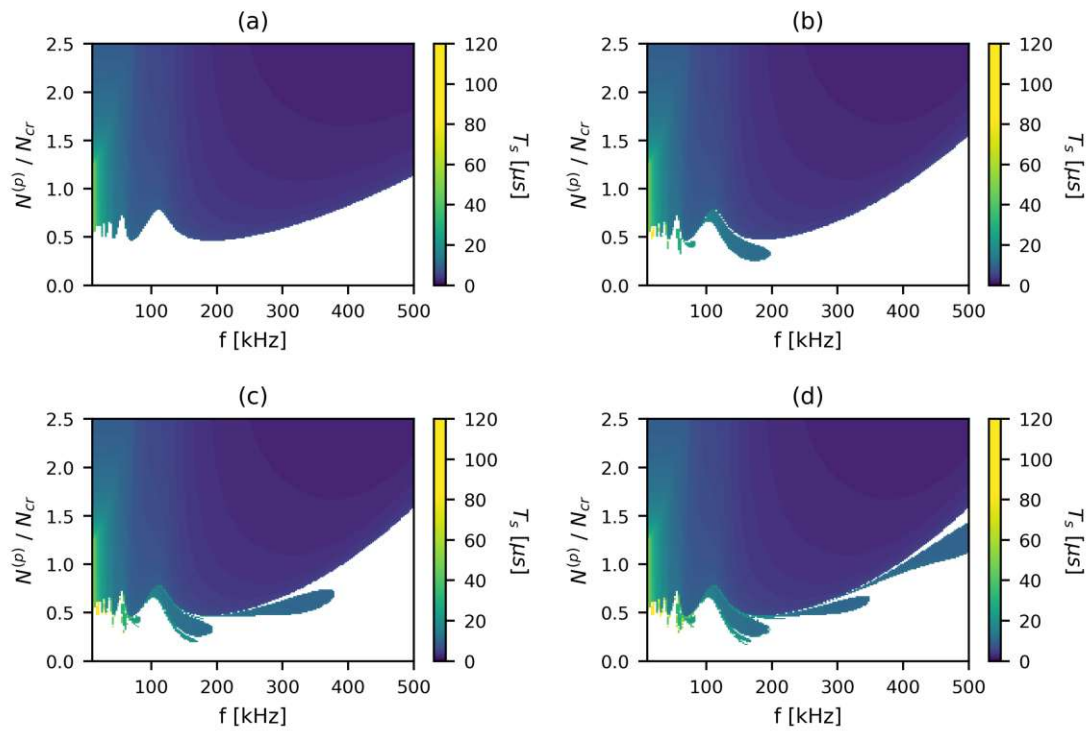


Figure 6.15: Maps of the initial snap-through time for different for $N^{(0)} = 2.5N_{cr}$ and one (a), two (b), three (c) or four (d) rectangular excitation pulses.

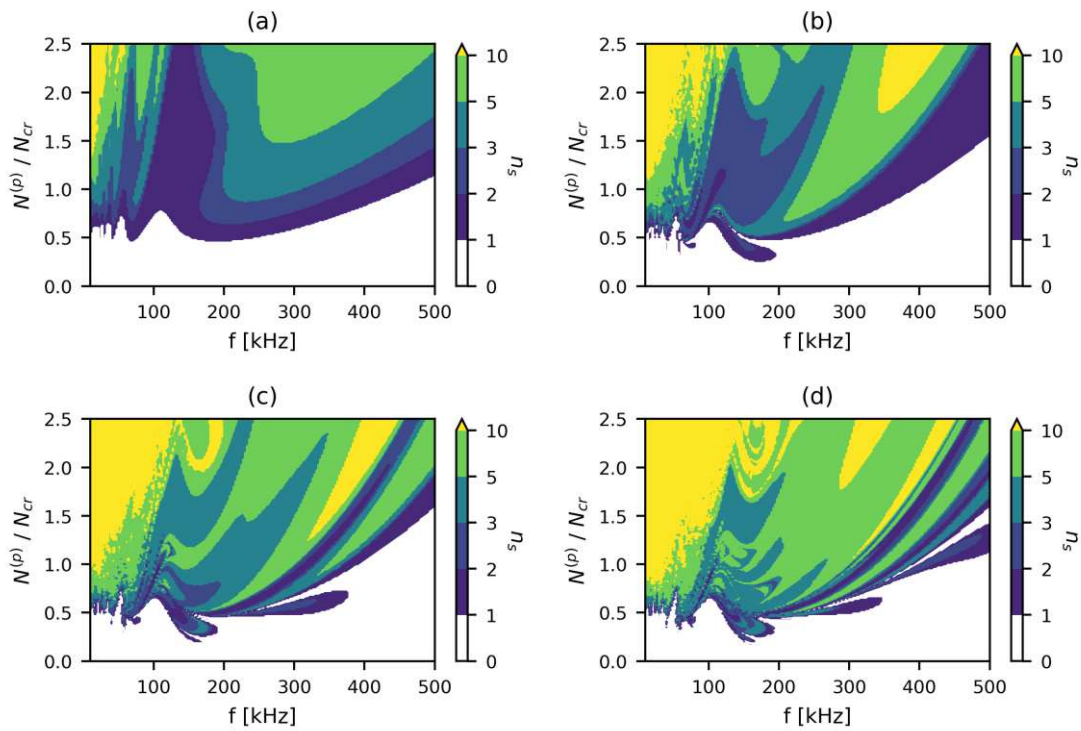


Figure 6.16: Number of switching events after $400 \mu\text{s}$ for $N^{(0)} = 2.5N_{cr}$ for one (a), two (b) three (c) and four (d) rectangular excitation pulses.

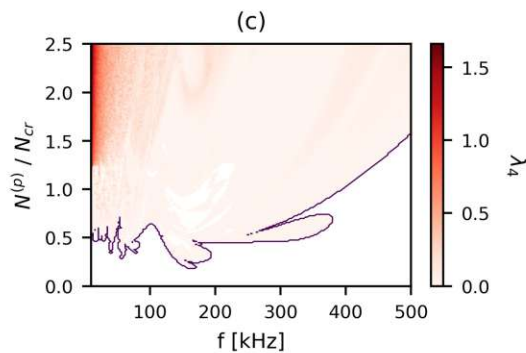


Figure 6.17: Modal participation factor λ_4 for three rectangular excitation pulses at $N^{(0)} = 2.5N_{cr}$

As mentioned above, the rectangular pulse train used in experiments had an offset added to the signal. We redefine the used pulse train as

$$N^{(p)}(t) = N_0^{(p)} [1 + \text{rect}(2\pi ft)\Pi_n(t, f)] \quad (6.8)$$

again using (6.7). The excitation signal is now positive during the whole pulse train. This means the piezoelectric transducer is now only used to increase the compressive stress in the membrane. The offset can also be interpreted as a static increase of the pre-stress for the duration of the pulse train. In figure 6.18 we again show initial snap-through time maps for one to four excitation pulses. Adding an offset to the pulse train has a large impact on the initial snap-through time map. While without offset there was one large connected area in figure 6.15(a) we now see multiple tongues divided by areas where no snap-through is possible at all in figure 6.18(a). The effect of adding more pulses remains largely the same

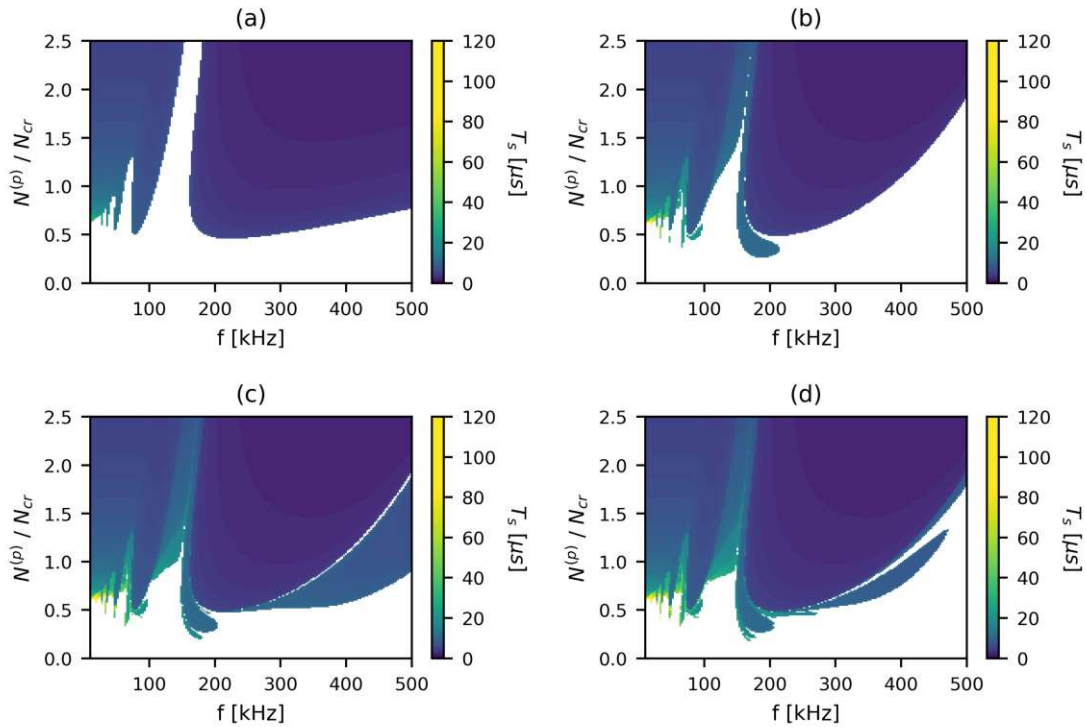


Figure 6.18: Maps of the initial snap-through time for $N^{(0)} = 2.5N_{cr}$ and one (a), two (b), three (c) or four (d) rectangular excitation pulses with offset.

as new regions with higher snap-through times get added to the map while the

excitation amplitudes needed decrease. We further observe a slight shift of the resonance frequency. If we interpret the static offset as an increase in pre-stress for the duration of the pulse train this immediately makes sense, since added pre-stress leads to a higher resonance frequency. Because the offset grows with the excitation amplitude $N_0^{(p)}$ the shift in resonance frequency will also grow with the excitation amplitude. The added offset however does not have the benefit of lowering the excitation amplitude $N_0^{(p)}$ needed in order to induce snap-through. This at first seems counter intuitive, since the added offset effectively doubles the maximum amplitude the excitation signal $N^{(p)}(t)$ reaches. However, if we again interpret the offset as an increase in static pre-stress for the duration of the excitation, we notice that this offset in pre-stress also increases the potential barrier that needs to be overcome by the oscillations. Looking at fig. 6.19, which again shows the number of

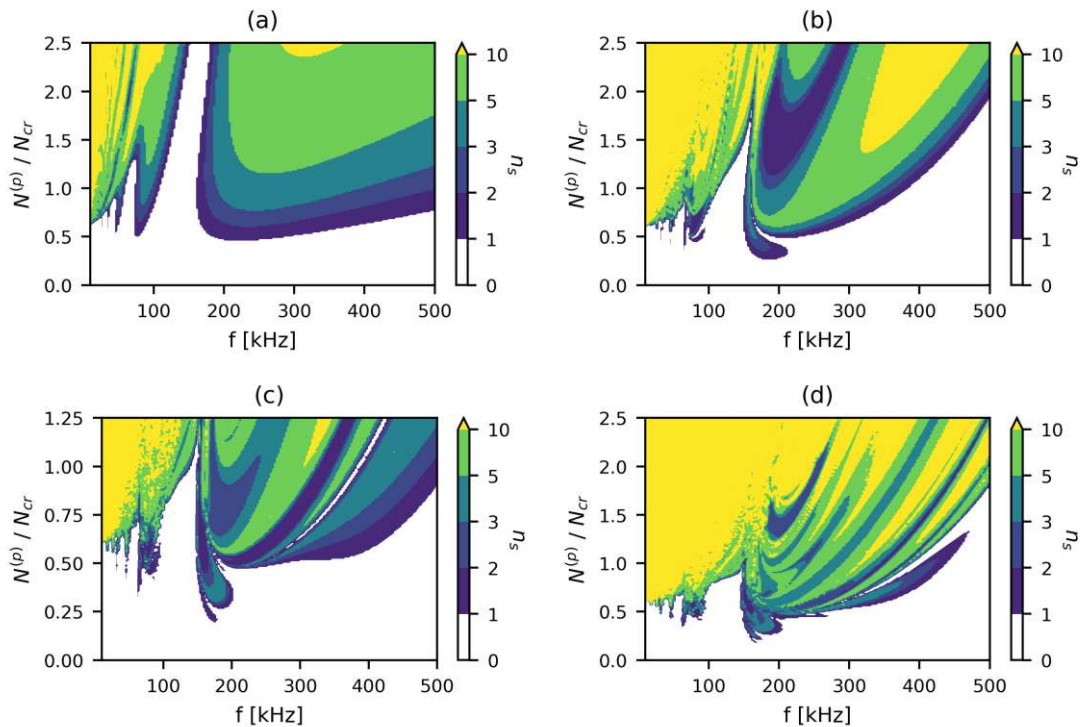


Figure 6.19: Number of switching events after $400 \mu\text{s}$ for $N^{(0)} = 2.5N_{cr}$ for one (a), two (b) three (c) and four (d) rectangular excitation pulses with offset.

switching events n_s observed during a $400 \mu\text{s}$ time period, we see a general increase in the observed number of snap-through events. Especially the areas with ten or

more snap-through events grow significantly compared to the images we see in figures 6.12 and 6.16.

We can summarize, that the choice of excitation signal has a major impact on the membrane dynamics. Full control over the number of snap-through events and consequently the buckling state of the plate can be achieved by applying a finite number of excitation pulses and letting the transients die out before inducing the next snap-through event. However waiting for the transients to die out limits the maximum switching frequency achievable by bistable MEMS actuators. For continuous excitation it could therefore be worthwhile to investigate more complex excitation signals.

Chapter 7

Conclusion and Future Work

In this thesis, we established a model to study the snap-through dynamics of piezoelectrically excited bistable MEMS plates. The model is based on the von Karman plate equation to account for the finite plate displacements during snap-through events. We obtain an approximate solution to the von Karman plate equation using Galerkin's method, which results in a set of coupled nonlinear differential equations. These equations represent the equations of motion of all considered vibrational modes. We numerically integrate the equation system to study the snap-through dynamics of a plate with a typical MEMS geometry. This approach allows for investigating the complex behavior of this nonlinear system at a low computational cost compared to other methods like FEM models.

Our results reveal that several trade-off decisions have to be made for the design of bistable MEMS. An important parameter in designing bistable MEMS is the mechanical static pre-stress in the system. While an increased pre-stress enables higher static deflections, this study finds the snap-through dynamics become significantly more complex and multi-modal for higher levels of pre-stress. The pre-stress also changes the systems resonance frequency and the excitation amplitudes needed in order to induce snap-through.

For the use of MEMS membranes as actuators precise control of the switching process is needed. In experiments switching was achieved by applying a finite pulse train to a piezoelectric layer on the membrane [4]. This causes a periodical change of the mechanical stress in the membrane, leading to oscillations of the membrane deflection. We analyze the effects of applying finite pulse trains with different

numbers of pulses and different wave forms as an excitation signal. Applying only a small number of excitation pulses drastically reduces the influence of higher order modes. While increasing the number of excitation pulses reduces the amplitudes needed in order to induce snap-through, the snap-through dynamics become more complex with each added pulse. The margins of error for inducing a well-controlled number of snap-through events decrease. This increases the influence of deviations in the excitation signal or environmental conditions, impacting the reliability of the snap-through process negatively.

While this work involves several simplifications in the mathematical model of the plate, important general findings can still be drawn for the design of bistable MEMS systems. The trade-offs regarding the influence of pre-stress provide the challenge to control this parameter in the fabrication process. The presented model can be used to study more complex excitation signals in an effort to gain further control over the dynamics at play. The model can further be refined to account for more details of real experiments. For the bistable MEMS membranes described by Dorfmeister et al. [4] this could be achieved by considering the anisotropy of silicon or adapting the model to describe circular geometries. The results presented here therefore not only provide valuable general insights into the snap-through dynamics of bistable MEMS, but can also form a basis for more sophisticated models.

Appendix A

ODE coefficients

Table A.1: The coefficients for the ODE system in (4.23) for $N = 4$ used in the simulations in chapter 6. The coefficients $G_{ijkl}^{(3)}$ are equal for all i .

Coefficient	Expression	Coefficient	Expression	Coefficient	Expression
M_{11}	$\frac{9}{4}L^2$	$C_{11}^{(y)}$	$3\pi^2$	$G_{223}^{(2)}$	$\frac{409403\pi^4 Eh}{11264L^2}$
M_{22}	$\frac{3}{2}L^2$	$C_{22}^{(y)}$	$\frac{15\pi^2}{2}$	$G_{224}^{(2)}$	$\frac{876173\pi^4 Eh}{22912L^2}$
M_{33}	$\frac{3}{2}L^2$	$C_{33}^{(y)}$	$2\pi^2$	$G_{331}^{(2)}$	$\frac{32023\pi^4 Eh}{1432L^2}$
M_{44}	L^2	$C_{44}^{(y)}$	$5\pi^2$	$G_{332}^{(2)}$	$\frac{409403\pi^4 Eh}{11264L^2}$
K_{11}	$\frac{32\pi^4}{L^2}$	$G_{11}^{(1)}$	$\frac{9\pi^4 Eh}{L^2}$	$G_{334}^{(2)}$	$\frac{876173\pi^4 Eh}{22912L^2}$
K_{22}	$\frac{179\pi^4}{2L^2}$	$G_{22}^{(1)}$	$\frac{961\pi^4 Eh}{64L^2}$	$G_{441}^{(2)}$	$\frac{889\pi^4 Eh}{132L^2}$
K_{33}	$\frac{179\pi^4}{2L^2}$	$G_{33}^{(1)}$	$\frac{961\pi^4 Eh}{64L^2}$	$G_{442}^{(2)}$	$\frac{876173\pi^4 Eh}{22912L^2}$
K_{44}	$\frac{132\pi^4}{L^2}$	$G_{44}^{(1)}$	$\frac{49\pi^4 Eh}{16L^2}$	$G_{443}^{(2)}$	$\frac{876173\pi^4 Eh}{22912L^2}$
$C_{11}^{(x)}$	$3\pi^2$	$G_{112}^{(2)}$	$\frac{32023\pi^4 Eh}{1432L^2}$	$G_{ijkl}^{(3)}$	$\frac{2670671\pi^4 Eh}{63008L^2}$
$C_{22}^{(x)}$	$2\pi^2$	$G_{113}^{(2)}$	$\frac{32023\pi^4 Eh}{1432L^2}$		
$C_{33}^{(x)}$	$\frac{15\pi^2}{2}$	$G_{114}^{(2)}$	$\frac{889\pi^4 Eh}{132L^2}$		
$C_{44}^{(x)}$	$5\pi^2$	$G_{221}^{(2)}$	$\frac{32023\pi^4 Eh}{1432L^2}$		

List of Figures

3.1	Bistable membrane stable ground states	5
3.2	Membrane material stack	6
3.3	Comparison between parametric and harmonic oscillator.	8
3.4	Stress components acting on an infinitesimal cube	9
3.5	One-dimensional strain sketch	9
3.6	Rectangular plate geometry	11
3.7	Thickness integrated forces of a rectangular plate	14
3.8	Shear forces and thickness integrated moments of a rectangular plate	14
4.1	Mode shapes ϕ_1, ϕ_2, ϕ_3 and ϕ_4 for a clamped rectangular plate	21
5.1	Comparison of simulation results for different solvers with $\text{rtol}=10^{-6}$	30
5.2	Comparison of simulation results for different solvers with $\text{rtol}=10^{-9}$	31
5.3	Convergence of numerical integration algorithms	32
5.4	Cumulative error over time compared to Radau with $\text{rtol}=10^{-12}$. . .	33
5.5	Cumulative error after 400 μs of integration time for decreasing rtol values compared to Radau with $\text{rtol}=10^{-12}$	33
5.6	Algorithm execution times for decreasing values of rtol	34
6.1	Static deflection amplitudes of the first four modes for static pre-stress values of $0 \leq N^{(0)} \leq 5N_{\text{cr}}$	37
6.2	Elastic potential energy for $0 \leq N^{(0)} \leq 3N_{\text{cr}}$	38
6.3	Initial snap-through time for $N^{(0)} = 1.1N_{\text{cr}}$	40
6.4	Zoom into the border region of the first tongue in fig. 6.3.	40
6.5	Example time series of the modal maximum deflections $w_i(t)$	41
6.6	Modal participation factors λ_i for the data in fig. 6.3	43
6.7	Maps of the initial snap-through time for static pre-stresses from $N^{(0)} =$ $1.5N_{\text{cr}}$ to $N^{(0)} = 3.0N_{\text{cr}}$	44
6.8	Zoom-ins into the initial snap-through time map in fig. 6.7c	45
6.9	Modal participation factor λ_4 for increasing levels of pre-stress	46

6.10	Example modal time series for $N^{(0)} = 3.0N_{cr}$, $f_p = 200$ kHz, $N^{(p)} = 0.3N_{cr}$	46
6.11	Maps of the initial snap-through time for $N^{(0)} = 2.5N_{cr}$ and one to four harmonic excitation pulses	48
6.12	Number of switching events after $400 \mu\text{s}$ for $N^{(0)} = 2.5N_{cr}$ and one to four harmonic excitation pulses	49
6.13	Modal participation factor λ_4 for three harmonic excitation pulses at $N^{(0)} = 2.5N_{cr}$	50
6.14	Example simulation results for an excitation with three harmonic pulses	50
6.15	Maps of the initial snap-through time for different for $N^{(0)} = 2.5N_{cr}$ and one to four rectangular excitation pulses	52
6.16	Number of switching events after $400 \mu\text{s}$ for $N^{(0)} = 2.5N_{cr}$ and one to four rectangular excitation pulses	53
6.17	Modal participation factor λ_4 for three rectangular excitation pulses at $N^{(0)} = 2.5N_{cr}$	53
6.18	Maps of the initial snap-through time for $N^{(0)} = 2.5N_{cr}$ and one to four rectangular excitation pulses with offset	54
6.19	Number of switching events after $400 \mu\text{s}$ for $N^{(0)} = 2.5N_{cr}$ and one to four rectangular excitation pulses with offset	55

List of Tables

6.1	Simulation parameters	35
A.1	Coefficients for the ODE system used for the simulations in chapter 6	59

Bibliography

- [1] Y. Chandra, I. Stanciulescu, L. N. Virgin, T. G. Eason, and S. M. Spottswood. A numerical investigation of snap-through in a shallow arch-like model. *Journal of Sound and Vibration*, 332(10):2532–2548, may 2013.
- [2] J. Dolbow and M. Gosz. Effect of out-of-plane properties of a polyimide film on the stress fields in microelectronic structures. *Mechanics of Materials*, 23(4):311–321, aug 1996.
- [3] M. Dorfmeister. *Piezoelectrically Actuated Bistable MEMS Membranes for Acoustic Applications*. PhD thesis, Technische Universität Wien, Vienna, AT, Aug. 2020.
- [4] M. Dorfmeister, B. Kössl, M. Schneider, G. Pfusterschmied, and U. Schmid. Switching performance of bistable membranes activated with integrated piezoelectric thin film transducers. *Journal of Micromechanics and Microengineering*, 29(10):105008, aug 2019.
- [5] M. Dorfmeister, M. Schneider, and U. Schmid. 3d characterisation of piezoelectric bistable MEMS membranes during switching. *Sensors and Actuators A: Physical*, 298:111576, oct 2019.
- [6] S. A. Emam and M. M. Abdalla. Subharmonic parametric resonance of simply supported buckled beams. *Nonlinear Dynamics*, 79(2):1443–1456, oct 2014.
- [7] S. Ilanko. Vibration and post-buckling of in-plane loaded rectangular plates using a multiterm galerkin’s method. 69(5):589–592, aug 2002.
- [8] B.-H. Kim, S.-I. Kim, J.-C. Lee, S.-J. Shin, and S.-J. Kim. Dynamic characteristics of a piezoelectric driven inkjet printhead fabricated using mems technology. *Sensors and Actuators A: Physical*, 173(1):244–253, 2012.

- [9] K. D. Murphy, L. N. Virgin, and S. A. Rizzi. The effect of thermal prestress on the free vibration characteristics of clamped rectangular plates: Theory and experiment. 119(2):243–249, apr 1997.
- [10] N.-T. Nguyen, X. Huang, and T. K. Chuan. MEMS-Micropumps: A Review . *Journal of Fluids Engineering*, 124(2):384–392, 05 2002.
- [11] S. Rajasekar and M. A. F. Sanjuan. *Nonlinear Resonances*. Springer International Publishing, 2016.
- [12] J. N. Reddy. *Theory and Analysis of Elastic Plates and Shells*. CRC Press, nov 2006.
- [13] L. N. Virgin. *Vibration of Axially Loaded Structures*. CAMBRIDGE, Aug. 2007.
- [14] D. Wang, C. Watkins, and H. Xie. Mems mirrors for lidar: A review. *Micro-machines*, 11(5), 2020.